Journal of Molecular Structure 1277 (2023) 134818

Contents lists available at ScienceDirect

Journal of Molecular Structure

journal homepage: www.elsevier.com/locate/molstr

Dithiocarbamates and dithiocarbonates containing 6-nitrosaccharin scaffold: Synthesis, antimycobacterial activity and *in silico* target prediction using ensemble docking-based reverse virtual screening

Muhammed Trawally[a,b], Kübra Demir-Yazıcı[a,b], Serap İpek Dingiş-Birgül[c], Kerem Kaya[d], Atilla Akdemir[c], Özlen Güzel-Akdemir[b,*]

[a] Department of Pharmaceutical Chemistry, Institute of Graduate Studies in Health Sciences, Istanbul University, Fatih, 34126, Istanbul, Turkey
[b] Department of Pharmaceutical Chemistry, Faculty of Pharmacy, Istanbul University, Fatih, 34116, Istanbul, Turkey
[c] Computer-Aided Drug Discovery Laboratory, Department of Pharmacology, Faculty of Pharmacy, Bezmialem Vakif University, Fatih, 34093, Istanbul, Turkey
[d] Department of Chemistry, Istanbul Technical University, Istanbul, Turkey

ARTICLE INFO

Article history:
Received 15 July 2022
Revised 14 December 2022
Accepted 17 December 2022
Available online 17 December 2022

Keywords:
Nitrosaccharin
Dithiocarbamate
Dithiocarbonate
Antimycobacterial
Ensemble docking
Reverse docking

ABSTRACT

Tuberculosis is a curable disease that costs the lives of 1.5 million people per year. It continues to pose a threat to global public health owing to the prevalence of multi-drug resistant (MDR) *Mycobacterium tuberculosis* strains which make its eradication a continuous challenge. To explore novel and effective antimycobacterial agents, a series of dithiocarbamates/dithiocarbonate-nitrosaccharin hybrids were prepared, characterized by spectral analyses, and assessed for their antimycobacterial activity against *M.tuberculosis* strain H37Rv. Some compounds showed activity with a minimum inhibitory concentration (MIC) of 0.45–6.09 μg/mL. Reverse ensemble docking against nine putative targets with fifteen different crystal structures was conducted to understand the mechanism of action of the most potent compound 6g. The *in silico* studies suggested enoyl ACP-reductase (InhA) and polyketide synthase 13 (Pks13) as possible targets for compound 6g.

1. Introduction

Tuberculosis (TB) is a curable contagious disease caused by *Mycobacterium tuberculosis* that infected10 million people and killed 1.5 million in 2020 [1]. Treatment of TB requires 3–4 drugs for 6 months [2–4]. The UN Sustainable Development Goals (SDG) for TB aims at a 90% reduction in TB-related mortality by 2030 [5]. However, attaining this is challenging due to the widespread presence of multidrug-resistant (MDR) and extensively drug-resistant (XDR) TB that have rendered the arsenal of anti-TB agents less active or even inactive [6]. If the TB SDG target is not met by 2030, it will kill 5.1 million and cost the world economy $3 trillion by 2045 [5]. To combat antimycobacterial resistance, scientists are searching for safer and cheaper novel agents with different mechanisms of action [2,3,7].

Dithiocarbamate and dithiocarbonates are sulfur-containing dithioates with similar backbones. Dithioates have a wide spectrum of biological actions due to the sulfur's nucleophilic and redox characteristics, attracting the attention of drug experts [8,9]. Dithioates are employed as precursors, linkers, and amine-protecting groups [10]. Dithiocarbamateis an important structural component in the natural compound brassinin that has anticancer properties, and in synthetic compounds like disulfiram and sulforamate that treat alcoholism and prevent cancer development, respectively (Fig. 1) [10]. Dithiocarbamates are used in drug development because of their versatility, lipophilicity, and ability to be bioisosterically modified. [11–13]. Their hybridization with essential scaffolds and antibiotics, such as ciprofloxacin and monobactam [14]; and the formation of complexes with transition metals have manifested antibacterial [14–18], antimycobacterial [13], antifungal [17–19], antileishmanial [20] and anticancer activities [11,21]. In addition, dithiocarbamates inhibit carbonic anhydrase, cholinesterase [22], and α-Glucosidase enzymes [23]. On the other hand, dithiocarbonates, known as xanthates, are used as precursors to scaffolds like lactams and indoles [24]. Beside xanthates have antibacterial [25], antimycobacterial [13], antifungal [25], and anticancer [13,26] as well as herbicidal and pesticidal activities [27]. Xanthates are also reported as carbonic anhydrase and tyrosinase inhibitors [28,29].

* Corresponding author.
E-mail address: oguzel@istanbul.edu.tr (Ö. Güzel-Akdemir).

https://doi.org/10.1016/j.molstruc.2022.134818
0022-2860/

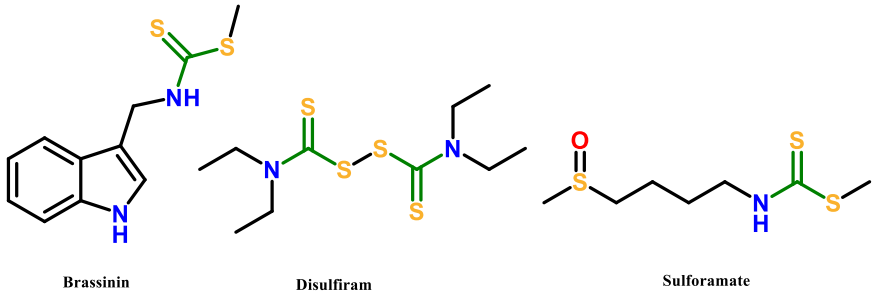

Fig. 1. Structures of compounds containing dithiocarbamates.

Saccharin, one of the oldest artificial-noncaloric sweeteners used in the food and drug industry as an alternative to sugar, has enjoyed being a subject of great interest in pharmaceutical chemistry [30]. In addition to antibacterial [31,32], antimycobacterial, anticancer [13], antiviral [33], antioxidant activities [31], saccharin analogs, inhibit carbonic anhydrase [34], interferon [35], human leukocyte elastase, cathepsin G, proteinase 3 [36], and rhomboid intramembrane protease enzymes [37].

In past decades, the exploration of promising druggable targets has earned paramount importance in the search for novel and effective drugs, particularly antimycobacterial drugs for combating antimycobacterial resistance. Antimycobacterial proteins absent in humans, such as enoyl-acyl carrier protein (ACP) reductase (InhA), polyketide synthase (Pks13), salicylate synthase (MbtI), 3-oxoacyl-[acyl-carrier-protein] synthase 1 (KasA), fatty acid degradation protein D32 (FadD32), 3-dehydroquinate dehydratase (AroQ), (3R)-hydroxyacyl-ACP dehydratase heterodimer (HadAB), prenylphosphoryl-beta-D-ribose oxidase (DprE1), and trehalose monomycolate transporter (Mmpl3) are promising druggable targets crucial for the survival of *M. tuberculosis* [38,39].

Structure-based virtual screening (SBVS) uses molecular docking to identify potential molecules in a chemical library that can bind to a target [40,41]. Molecular docking predicts the binding mode and affinity of a ligand-based on ligand-protein complementarity using a scoring function [41–43]. Thus, detailed information on the 3D structure of a particular target protein eases the determination of a particular scaffold with appropriate substituents, thereby generating potential hits that can eventually be synthesized. SBVS is not applicable if the synthesized compounds are tested in bioactivity assays directly without performing binding or inhibition assays against the target [44]. In this situation, reverse virtual screening (RVS) or reverse docking studies are appropriate and advantageous approaches. In short, the most active compounds are docked into a set of putative target proteins to identify the most likely target(s) for the tested compounds [43,45]. Also, RVS vastly contributes to revealing the target of present drugs with unknown mechanisms of action and to drug repurposing of clinically approved drugs [43,45,46]. At the same time, RVS encounters a limitation of docking compound(s) to a single rigid structure of a target protein which could have different conformations due to different rotamers of amino acids [41,47,48]. To address this problem, an ensemble of different conformations of a target protein(s) is used in docking to simulate the induced-fit-based conformational changes or protein flexibility [41,48].

Here, we report the synthesis and antimycobacterial activity of 11 novel dithioate-nitrosaccharin derivatives. To investigate the putative target of the most potent compound, **6g**, we conducted a reverse virtual screening against 9 different target proteins, and we utilized ensemble docking to address different structures of InhA due to the presence of different rotamers of some amino acids in the binding site.

2. Results and discussion

2.1. Chemistry

The compounds were successfully prepared via multistep synthesis as depicted in Scheme 1. 2-methyl-5-nitrobenzenesulfonamide **(2)** was prepared according to a previously reported method in the literature [49]. Cranwell et al. communicated the synthesis of 6-nitrosaccharin **(3)** by heating compound **2** in H_2SO_4 at 65–70 °C [50]. However, this method was not successful, and thus, we increased and maintained the temperature at 75–80 °C. The methyl group of compound **2** was oxidized to carboxylic acid using chromium(VI)oxide and then cyclocondensed to give compound **3.** Although the purification of compound **2** leads to a low yield, we realized that compound **3** could only be obtained with a considerable yield of at least 50% using pure compound **2**.

In the subsequent step, 6-nitrosaccharin **(3)** was successfully hydroxymethylated with formaldehyde to give a good yield of compound **4**. Again, our attempt of chlorinating compound **4** with $SOCl_2$ in ether to obtain **5** encountered difficulties and ended with side products and low yield. We assume this was due to the excess $SOCl_2$ left in the reaction mixture. To avoid this, we decided to eradicate $SOCl_2$ by either adding a base or keeping the reaction mixture open for a long period to facilitate the removal of $SOCl_2$. However, only the latter accomplished the removal of $SOCl_2$. In the final step, we first tried to synthesize our target compounds **6a-g** by refluxing compound **5** with potassium dithiocarbamate derivatives in ethanol. This procedure only afforded compound **6g.** Interestingly, when we replaced ethanol with acetone, compounds **6a-g** and **7a-d** were successfully obtained (Scheme 1). The structures of all newly synthesized compounds were confirmed by NMR and IR spectra (See Supplementary, **Figs. S1-S52**).

In the FT-IR spectra of the new compounds **3–5, 6a-6g**, and **7a-7d**, the lactam C = O group on the nitrosaccharin ring signaled between 1747 and 1725 cm^{-1} as strong stretching bands. The asymmetric and symmetric *S = O* stretching vibrations of the sulfonamide group had absorption bands at the 1272–1259 cm^{-1} and 1188–1182 cm^{-1} areas, respectively. For compounds **6a-6g** and **7a-7d**, additional C = S stretching bands appeared between 1241 and 1211 cm^{-1} which point out the formed dithiocarbamate or dithiocarbonate functionality.

The ^1H NMR spectra of the intermediates **3–5**, dithiocarbamates **6a-6g**, and dithiocarbonates **7a-7d** showed common proton signals due to the main scaffold nitrosacharin ring. Starting from the downfield, the C_7 proton of the benzisothiazole rings was observed between δ 9.34–8.76 ppm as a *–meta* coupled doublet due to the interaction with the C_5 proton of the rings. The C_5 protons of the compounds resonated between δ 8.77–8.55 ppm as a doublet of doublet making both *–ortho* and *–meta* coupling with C_4 and C_7 protons, respectively. The C_4 protons of the common benzisothiazole interacted only with C_5 protons and appeared doublets

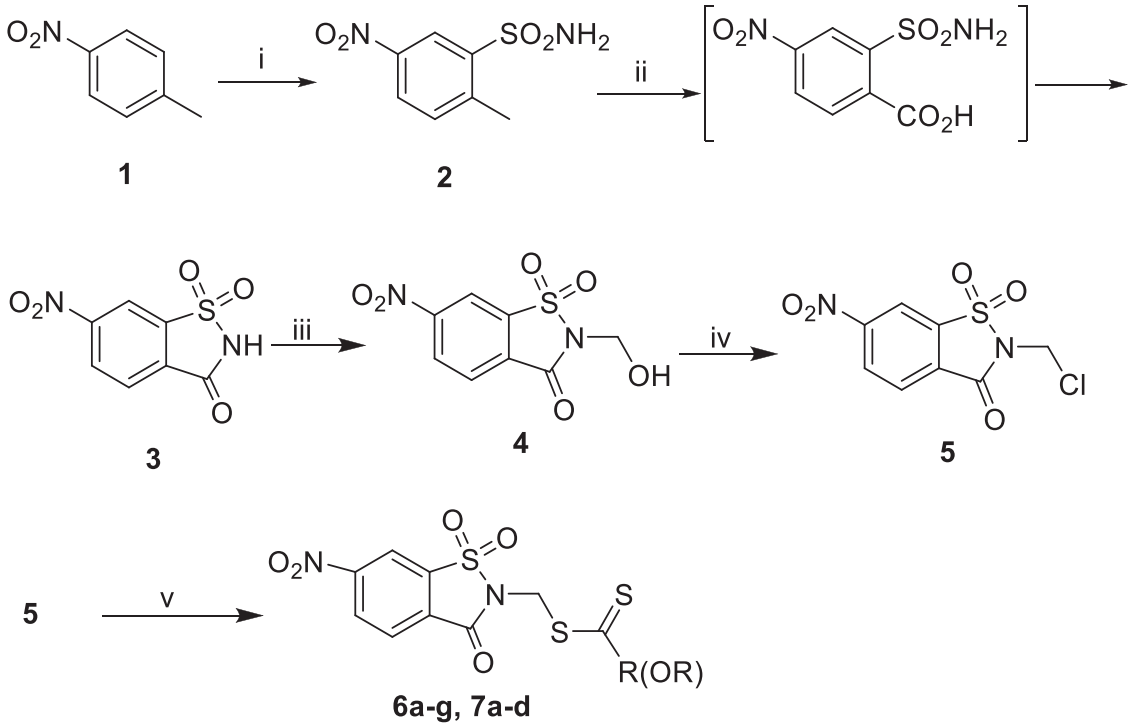

Scheme 1. Preparation of (6-nitro-1,1-dioxido-3-oxo-1,2-benzisothiazol-2(3H)-yl) methyl N,N-disubstituted dithiocarbamate / O-alkyldithiocarbonate derivatives. Reagents and conditions: (i) $ClSO_3H$, NH_3; (ii) CrO_3, H^+; (iii) 37% HCHO, EtOH, 0 °C, 16 h; (iv) ether, $SOCl_2$, 0 °C, 24 h; (v) RCS_2K/ $ROCS_2K$, EtOH, reflux, 1 h.

between δ 8.40–8.04 ppm. The methylene protons of –N–CH_2-S– groups were detected as singlets at δ 5.87–5.48 ppm for dithiocarbamates **6a-6g**, and dithiocarbonates **7a-7d** Similarly, intermediates **4** and **5** signaled singlets at δ 5.22 and δ 5.87 ppm due to their –N–CH_2-O– and –N–CH_2-Cl group protons, respectively. Additionally, for compounds **3** and **4**, N–H and O–H protons were observed at δ 4.89 ppm, and δ 5.59 ppm as singlets, respectively. All the other peaks associated with other protons of newly synthesized compounds **6a-6g** and **7a-7d** were observed in relevant regions due to their substitution patterns.

The ^{13}C NMR (APT and HSQC-2D) spectra of the new nitrosaccharin-based compounds **6a-6g** and **7a-7d** (except **6b** and **6d**) indicated that the carbon signals of the common C = S moiety were detected with the highest shift value, at δ 209.88–187.66 ppm, and the absence of these peaks for intermediates **3–5** was verified the dithiocarbamate or carbonate structures of newly synthesized compounds. Other carbons of the common nitrosacharin ring appeared usually starting from the C = O (δ 161.78–156.75 ppm) in order to C_6, C_{7a}, C_{3a}, C_5, C_4, and C_7 (between δ 152.93–117.32 ppm). The methylene carbons shifts of –N–CH_2– groups were detected between δ 63.90–42.44 ppm. To further structural analysis, HSQC-2D run on compounds **5, 6c, 6e, 6f**, and **7d** allowed the complete assignment of the proton and carbon NMR signals of substituted groups to the main scaffold, particularly (See Supplementary, **Figs. S1-S52**).

The molecular ions and fragmentations signals of the new compounds were determined with mass spectroscopies (APCI and ESI) which confirmed the exact mass of the compounds **6a-6f** and **7d**, and the main fragment hydroxyimino cation for compounds **7a**-**7c** (See Supplementary, **Figs. S1-S52**).

2.2. In vitro evaluation of antimycobacterial activity against M. tuberculosis *H37Rv*

The primary screen was conducted against *M. tuberculosis* H37Rv (ATCC 27294) in BACTEC 12B medium using a broth microdilution assay (MABA; Microplate Alamar Blue Assay) at the Tuberculosis Antimicrobial Acquisition and Coordinating Facility (TAACF) [51]. Compounds were tested in ten 2-fold dilutions, usually from 100 μg/mL to 0.19 μg/mL. Compounds demonstrating bacterial growth inhibition of at least 90% in the primary screen were retested against *M. tuberculosis* H37Rv to determine the actual minimum inhibitory concentration (MIC) in the MABA (Table 1**).** The MIC was defined as the lowest concentration effecting a reduction in fluorescence of 90% relative to controls. IC_{90} values of $\leq$ 10 μg/mL are considered active and seven compounds were identified of which compound **6g** is the most potent against *M. tuberculosis*.

Among the newly synthesized compounds, the dithiocarbamate derivate compound **6g** showed the best inhibitory activity against *M. tuberculosis* H37Rv with the lowest MIC values (IC_{90} = 0.450 μg/mL, shown in Table 1; IC_{50} = 0.400 μg/mL, not shown). Although a clear structure-activity relationship could not be determined, it can be inferred that dithiocarbamate derivatives are more active in mycobacterial growth inhibition assays than dithiocarbonate derivatives. For dithiocarbamate **6a-6g**, bearing open alkyl chains (i.e. compounds **6a** and **6b**) or bulky groups like benzylpiperazine (i.e. compound **6e,** IC_{90}> 100 μg/mL, shown in Table 1; and IC_{50}= 75.740 μg/mL, not shown) resulted in decreasing antitubercular activity. Conversely, compounds substituted with cyclic amines carrying small groups like compounds **6c, 6d, 6f**, and **6g** seem to be preferable for increasing the inhibitory potential. Among them, compound **6g** bearing the five-membered pyrrolidine maximized the activity. For dithiocarbonate derivatives **7a**-**7d**, again, substitutions with small residues increased inhibitory activity, and the worst inhibitory activity was detected for compound **7c** with a bulky pentyl chain, eventually (IC_{50}= 27.260 and IC_{90}= 60.970 μg/mL).

2.3. Molecular modeling studies to identify possible target proteins for observed MT growth inhibition data

Possible target proteins have first been identified from the literature and subsequently, a reverse ensemble docking study was per-

Table 1
In vitro antimycobacterial activity of compounds 6a-g and 7a-d has been shared as IC_{90} values.

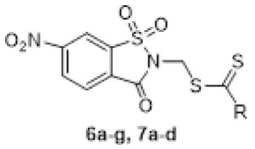

6a-g, 7a-d

Cpd.	R	IC_{90} (μg/mL)	Cpd.	R	IC_{90} (μg/mL)
6a	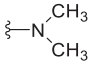	6.090	**7a**	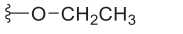	4.620
6b	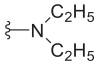	2.690	**7b**	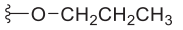	5.180
6c	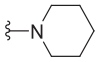	2.380	**7c**	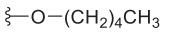	60.970
6d	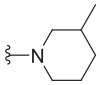	0.460	**7d**	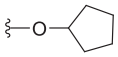	17.810
6e	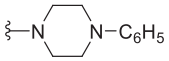	>100			
6f	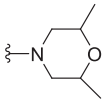	10.950			
6g		0.450			
Rifampin	–	0.125			

Table 2
Essential targets of M. Tuberculosis used in molecular modeling studies.

Protein Target	Function	PDB ID (Å)
Pks13	Mycolic acid biosynthesis	5V3X (1.94 Å)
KasA	Mycolic acid biosynthesis	6Y2I (1.53 Å)
FadD32	Mycolic acid biosynthesis	5HM3 (2.25 Å)
HadAB	Mycolic acid biosynthesis	4RLT (2.05 Å)
DprE1	Cell wall biosynthesis	4P8C (1.95 Å)
AroQ	Amino acid biosynthesis	2Y71 (1.50 Å)
Mmpl3	Mycolic acid transport	7C2N (2.82 Å)
Mbtl	Mycobactin biosynthesis	3VEH (2.00 Å)

formed for **6g**. Subsequently, selected protein-**6g** complexes were further investigated with MD simulations.

Target protein selection

A total of nine different proteins reported to be potential druggable targets, that are vital to the growth of *M. Tuberculosis,* were selected for reverse virtual screening (Table 2). One crystal structure was selected for each protein. However, seven different crystal structures were selected for InhA due to the presence of various high-resolution cocrystal structures and significant conformational differences in the residues of the active site (Table 3).

These seven InhA crystal structures showed differences in the sidechain conformations of especially Phe149 and Tyr158, the Helix H6 conformation, and the presence or absence of the NAD cofactor (Fig. 2). Phe149 and Tyr158 can be either pointing towards the ligand enabling binding interactions ("*in*" position) or away from the ligand creating additional space in the active site ("*out*" position). Helix H6 (residues 196–206) is located near the active site and affects the binging modes of ligands. It can be either pointing towards the active site and narrowing it ("closed" state) or away from the active site making its volume larger ("open" state). The InhA crystal structures were superimposed on Cα-atoms. The RMSD for the NAD-containing InhA structures (4BQP, 4UVG, 3FNG, 4D0R) with reference to 4TZK was between 0.24 Å and 0.98 Å (268 Cα-atoms) while for the apo structure 4BGE with respect to 4BGE it was 0.62 Å (268 Cα-atoms).

InhA (PDB: 3FNG) has Phe149 in the *out* position, Tyr158 in the *in* position which forms a hydrogen bond with the ligand, the NAD cofactor present which forms a hydrogen bond with the ligand, and helix H6 closed (purple in Fig. 2). InhA (PDB: 4UVG) has both Phe149 and Tyr158 in the *out* position, helix H6 open, and the NAD cofactor present which forms a hydrogen bond with the ligand (turquoise in Fig. 2). InhA (PDB: 4TZK) has Phe149 in the *out* position, Tyr158 in the *in* position which forms a hydrogen bond with the ligand, helix H6 open, and the NAD cofactor present which forms a hydrogen bond with the ligand (chartreuse in Fig. 2). InhA (PDB: 4BQP) has both Phe149 and Tyr158 in the *out* position, helix H6 wide open, and the NAD cofactor present which forms a hydrogen bond with the ligand (orange in Fig. 2). InhA (PDB: 4D0R) has Phe149 in the *in* position which forms a π-π interaction with the phenyl ring of the ligand, Tyr158 in the *out* position, the NAD cofactor present which forms a hydrogen bond with the ligand, and helix H6 open (pink in Fig. 2) InhA (PDB: 4BII_D Chain) has Phe149 in the *out* position, Tyr158 in the *in* position which forms a hydrogen bond with the ligand, helix H6 wide open, and lacks NAD cofactor (green in Fig. 2). InhA (PDB: 4BGE) is a resistant Ser94Ala mutant form of 4BII and has Phe149 in the *out* position, Tyr158 in the *in* position which forms a hydrogen bond with the ligand, helix H6 wide open, and lacks NAD cofactor (grey in Fig. 2) [52].

Validation of docking protocols

The HTVS precision docking setting was first validated using retrospective docking studies in which the cocrystallized ligand was docked back into its respective active site. All binding poses as observed in the cocrystal structures could be reproduced with an RMSD value generally below 1.5 Å (See Supplementary, **Figs. S53-S57 & Table S68**).

Table 3
Different crystal structures of InhA of M. Tuberculosis used in molecular modeling studies.

Protein Target	Function	PDB ID (Å)	Differences in InhA structures
InhA	Mycolic acid biosynthesis	3FNG (1.97 Å)	Phe149 (out), Tyr158 (in), H6 closed, NAD
		4UVG (1.92 Å)	Phe149 (out), Tyr158 (out), H6 open, NAD
		4TZK (1.62 Å)	Phe149 (out), Tyr158 (in), H6 open, NAD
		4BQP (1.89 Å)	Phe149 (out), Tyr158 (out), H6 wide open, NAD
		4D0R (2.75 Å)	Phe149 (in) Tyr158 (out), H6 wide open, NAD
		4BII (1.95 Å)	Phe149 (out), Tyr158 (in), H6 wide open
		4BGE (2.25 Å)	Phe149 (out), Tyr158 (in), H6 wide open, S94A

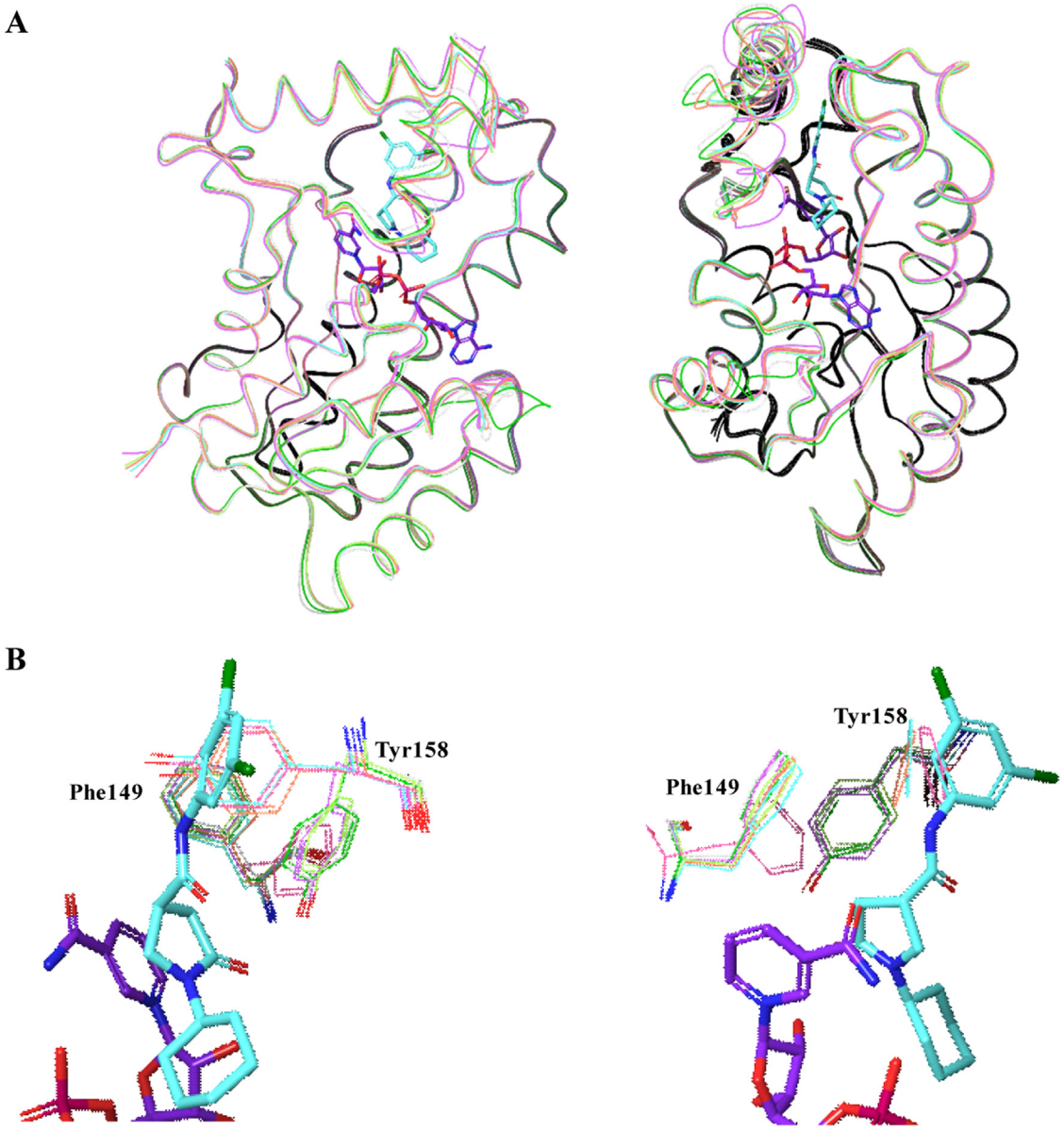

Fig. 2. A) The superposition of the seven InhA crystal structures that have been used in the docking procedure is shown in two different orientations. B) The binding poses of 1-cyclohexyl-N-(3,5-dichlorophenyl)−5-oxopyrrolidine-3-carboxamide (turquoise) and NAD (purple) in the active site of InhA (PDB: 4TZK) are shown in two different orientations.

Reverse docking studies

Compound **6g** shows the lowest IC_{90} value in the *M. tuberculosis* growth inhibition assays (Table 1). Reverse docking studies of this compound were performed against nine essential proteins of *M. tuberculosis* to investigate the possible target(s) for **6g**. Dockings were performed into an ensemble of fifteen different selected crystal structures, seven different structures for InhA and one structure for the other proteins (Tables 2 and 3), using HTVS precision. Subsequently, the docked poses were rescored using SP and XP precision. Although XP uses a more sophisticated scoring function than both HTVS and SP it may still not be reliable for selecting the best docking poses [53]. MM-GBSA rescoring of docking results has proven to be an effective approach in determining the best binding poses and ranking them [54]. As such, the MM-GBSA free bind-

Table 4
MM-GBSA binding energies as well the binding interactions of the docked pose of compound **6g** for each target crystal structure is shown. The poses with MM-GBSA docking scores that are lower than −40 kcal/mol are indicated in bold.

Target	PDB Code	MM-GBSA score (kcal/mol)	Type of interactions	Involved residues
Pks13	**5V3X**	**−51.56**	Hydrogen bond, π-π interaction, cation-π interaction	His1664, His 1699, Tyr1674
Mbtl	3VEH	−36.39	Hydrogen bond, cation-π interaction	Lys205, Thr271, Glu294, Lys438
KasA	6Y21	−38.65	–	–
FadD32	**5HM3**	**−40.38**	Hydrogen bond	Ser321
HadAB	4RLT	−30.32	–	–
DprE1	4P8C	−36.50	Hydrogen bond, cation-π interaction	Asn385, Lys418
AroQ	**2Y71**	**−44.33**	**Hydrogen bond**	**Tyr24**
Mmpl3	7C2N	−30.61	–	–
InhA	3FNG	−36.56	Hydrogen Bond	Met98, Tyr158
InhA	4UVG	−29.12	π-π interaction	Phe97
InhA	**4TZK**	**−62.10**	**Hydrogen bond, π-π interaction**	**NAD, Phe149**
InhA	4BQP	−38.94	Hydrogen bond	NAD
InhA	**4D0R**	**−71.61**	**Hydrogen bond, π-π interaction, cation-π interaction**	**NAD, Phe149, Tyr158**
InhA	**4BII**	**−55.58**	**Hydrogen bond, π-π interaction**	**Tyr158, Ile194, Phe149**
InhA	**4BGE**	**−55.37**	**Hydrogen bond**	**Tyr158, Ile21, Ile194**

ing energies of the docked poses were calculated (Table 4). The MM-GBSA results of Pks13–**6g** (5V3X), FadD32–**6g** (5HM3), AroQ-**6g** (2Y71), InhA-**6g** (4BGE), InhA-**6g** (4TZK), InhA-**6g** (4D0R) and InhA-**6g** (4BII) complexes were selected for molecular dynamics simulations. The obtained protein-**6g** complexes with a calculated binding free energy of −40 kcal/mol or better were subjected to a 250 ns molecular dynamics (MD) simulation to investigate whether the interactions between the ligand and the protein are sustained throughout the simulation.

Molecular dynamics simulations

The Pks13–**6g**, FadD32–**6g**, AroQ-**6g** and InhA-**6g** (only for 4BGE, 4TK, 4D0R, 4BII) complexes as obtained with docking simulations have been selected for 250 MD simulations. The crystal structures in complex with their cocrystallized ligands were also simulated. These MD studies indicate that compound **6g** may bind with higher affinity to InhA (both with and without NAD) compared to Pks13 and FadD32. The AroQ-**6g** complex was not stable during the simulation and no significant ligand-protein binding interactions were observed (See Supplementary, **Fig. S69**).

The docked pose of Pks13–**6g** with an MM-GBSA binding free energy of −56.56 kcal/mol shows π-π interactions with the sidechains of Tyr1674 and His1699, a hydrogen bond with His1664, and a cation-π interaction with His1699 (Fig. 3A). The observed hydrogen bond with His1664 was not sustained during the 250 ns MD simulation, however, the carbonyl formed two new water-mediated hydrogen bonds with Ala1477 (25%) and Asn1640 (25%). In addition, other water-mediated hydrogen bonds were observed with Arg1563, Asp1644 and Tyr1674. The π-π and cation-π interactions with His1699, and π-π interaction with Tyr 1674 were present for 29% and 46% during the simulation, respectively (Fig. 3B). This indicates that the ligand was in continuous interaction with Tyr1674. Also, a new π-π interaction with His1663 was present for 56% of the simulation time and hydrophobic interaction with Phe1585 lasted for about half of the simulation time (Fig. 3C). The RMSD value of the protein Cα-atoms is in general lower than 2.8 Å indicating that the protein conformation is stable. The ligand RMSD value was generally below 3.2 Å indicating that the docked pose was stable during the course of the simulation (Fig. 3D). The average MM-GBSA binding free energy of the Pks13–**6g** complex was −61.88 +/- 3.44 kcal/mol (Table 5). The highest and lowest binding energies were −50 and −70 kcal/mol, respectively (Fig. 3E).

The MD simulation of Pks13 in complex with its cocrystallized ligand indicates that the hydrogen bonding between the ligand and Tyr1637 and Ile1643 are maintained throughout the simulation. The RMSD values of the protein Cα-atoms and the ligand were below 3.2 Å. The average MM-GBSA binding free energy was −72,30 +/- 4.05 kcal/mol. The highest and lowest binding energies were −60 and −87 kcal/mol, respectively (See Supplementary, **Fig. S70**). This suggests that compound **6g** may bind with lower affinity to Pks13 compared to the cocrystallized ligand.

The pyrrolidine ring has a short distance with Gln1633 and Phe1670 and constantly forms hydrophobic interaction. Aliphatic groups smaller than pyrrolidine do not continuously form hydrophobic contacts with Gln1633 and Phe1670 whiles long aliphatic chains and bulkier groups result in steric clashes. The nitro group interacts with the protein 28% of the simulation period.

The FadD32–**6g** complex (5HM3) with an MM-GBSA binding free energy of −40.38 kcal/mol shows a hydrogen bond formed between the carbonyl group on the nitrosacharrin ring and the backbone of Ser321 (Fig. 4A). However, this hydrogen bond was lost during the first 20 ns of the 250 ns MD simulation and the ligand moved away from the supposed binding site to form both direct and water-bridged hydrogen bonds with Gln505 (23%) and Arg611 (61%). A hydrogen bond and a water-bridged hydrogen bond were observed with Val397 and Ala488, respectively (Fig. 4B & 4C). The RMSD value of the protein Cα-atoms is in general lower than 2.8 Å indicating that the protein conformation is stable. The ligand RMSD value was generally below 5 Å in the first 150 ns and then gradually increases to 9 Å indicating that the ligand diffused away from the protein during the course of the simulation. (Fig. 4D). The average MM-GBSA binding free energy of the FadD32–**6g** complex was −61.88 +/- 3.44 kcal/mol. The highest and lowest binding energies were −45 and −70 kcal/mol respectively (Fig. 4E).

The MD simulation of FadD32 in complex with its cocrystallized ligand indicates that the hydrogen bonding between the ligand and Ser321, Ser349, and Asp476 are maintained throughout the simulation. The RMSD values of the protein Cα-atoms and the ligand were below 2.8 Å and 2.4 Å, respectively. The average MM-GBSA binding free energy was −112,02 +/- 7.02 kcal/mol. The highest and lowest binding energies were −90 and −130 kcal/mol respectively (See Supplementary, **Fig. S73**). The much higher average MM-GBSA binding energy over the 250 ns MD simulation for compound **6g** suggests that it may show a much weaker affinity for FadD32 compared to the cocrystallized ligand.

The MD simulation of AroQ-**6g** complex (2Y71) reveals that the hydrogen bonding interaction of the sulfonyl group of nitrosacharin with the sidechain of Tyr24 which was not sustained dur-

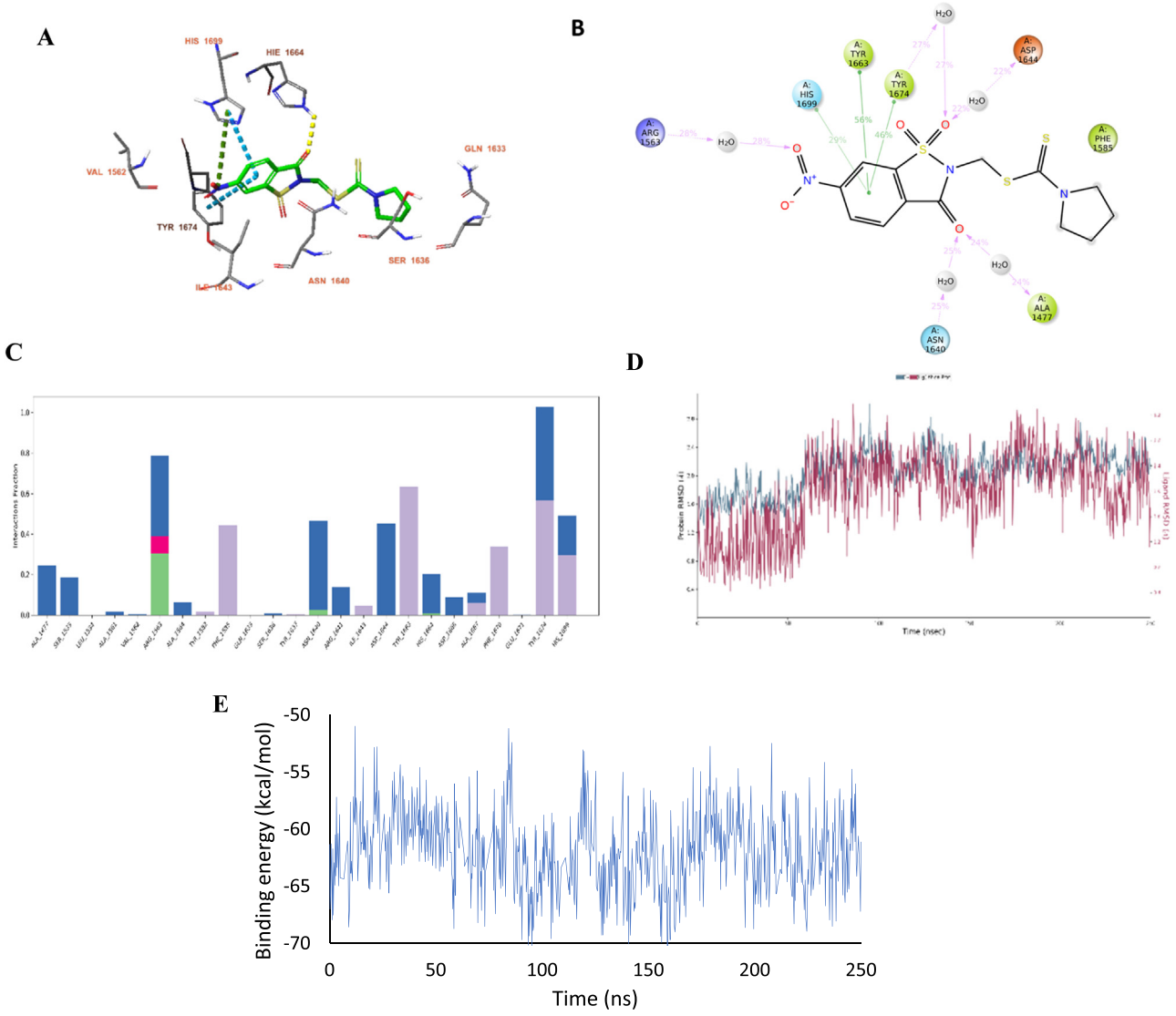

Fig. 3. A) The docked pose of compound **6g** in the active site of Pks13 (5V3X) Hydrogen bonds are indicated in yellow dashed lines. π-π stackings are indicated in turquoise and cation-π interactions are indicated in green dashed lines. B) The binding interactions during the 250 ns MD simulation. The interactions present for at least 20% of the MD simulation are shown. Hydrophobic amino acids are indicated in green, negatively charged amino acids are indicated in red, positively charged amino acids are indicated in purple and polar amino acids are indicated in blue. C) Protein-ligand contacts histogram. Green represents hydrogen bonds, blue represents water-bridged hydrogen bonds, grey represents hydrophobic interactions, and red represents ionic bonds. D) RMSD of the protein Cα-atoms (blue) and ligand (red). E) The Protein-ligand interaction energy (kcal/mol) during the MD simulation.

ing the MD simulation and that it was replaced by water-bridged and hydrophobic interactions during the MD simulation (**Fig. S69A** & **B**). The ligand frequently formed either an ionic bond, hydrogen bond, a water-bridged hydrogen bond, or π-cation interaction with Arg19 throughout the simulation (**Fig. S69C**). The RMSD value of the protein Cα-atoms is in general lower than 2 Å indicating that the protein conformation is stable. The ligand RMSD value fluctuates between 3 and 9 Å indicating that the ligand at some points diffused away from the protein during the first 150 ns and eventually stabilized around 3 Å in the last 70 ns of the simulation (**Fig. S69D**). The average MM-GBSA binding free energy of the AroQ-**6g** complex was −39.51 +/- 9.17 kcal/mol. The highest and lowest binding energies were −20 and −65 kcal/mol respectively (**Fig. S69E**).

The MD simulation of AroQ in complex with its cocrystallized ligand indicates that the hydrogen bonds between Asn75, Ile102, and Ser103 are maintained throughout the simulation. The RMSD values of the protein Cα-atoms were generally below 1.75 Å during the first 175 ns and thereafter increased to 2.25 Å. The ligand RMSD value was generally below 2.5 Å in the first 175 ns and thereafter increased to 5.6 Å. The average MM-GBSA binding free energy was −49,59 +/- 9.23 kcal/mol. The highest and lowest binding energies were −26 and −77 kcal/mol respectively (See Supplementary, **Fig. S72**).

InhA-**6g** complex (4BGE) having an MM-GBSA binding free energy of −55.37 kcal/mol formed three hydrogens with the sidechain of the crucial catalytic residue, Tyr158, backbones of Ile21 and Ile194 (Fig. 5A). During the 250 ns simulation, the hydrogen bond formed with Tyr158 was not maintained and shifted to another crucial catalytic residue, Lys165 (28%). The hydrogen bonding between the nitro group and Ile21 was continuous for 70% of the simulation time while the hydrogen bonding between the sulfonyl group and Ile194 (99%) was sustained throughout the simulation period. Also, hydrophobic interaction with Phe149 was observed for 80% of the simulation time (Fig. 5B & 5C). The RMSD value of the protein Cα-atoms was stabilized at 2.8 Å. The ligand

Table 5
The MM-GBSA binding energy obtained from the 250 ns MD simulations of the selected protein-ligand complexes.

	MM-GBSA (kcal/mol)	
Complex (PDB)	Cocrystallized ligand (affinity)[1]	Compound 6g
Pks13 (5V3X)	−72,30 +/- 4.05 (**IC_{50}: 260 nM**)[1]	−61.88 +/- 3.44
FadD32 (5HM3)	−112,02 +/- 7.03 (**IC_{50}: 6800 nM**)[1]	−55.26 +/- 4.11
AroQ (2Y71)	−49.59 +/- 9.23 (**K_i: 42.5 nM**)[1]	−39.51 +/- 9.17
InhA (4BII)	−274,26 +/- 15.36 (**K_i: 4800 nM**)[1]	−72.08 +/- 3.34
InhA (4BGE)	−94,65 +/- 9.34 (**K_i: 4800 nM**)[1]	−76.33 +/- 5.94; (−78.45 +/−3.90)[3]
InhA (4TZK)[2]	−81,45 +/- 7.14 (**IC_{50}: 390 nM**)[1]	−83.55 +/- 4.19
InhA (4D0R)[2]	−80.26 +/- 7.50 (**IC_{50}: not yet published**)	−75.19 +/- 3.76

[1] The binding affinity of the cocrystallized ligand according to BindingMOAD. [55,56].
[2] InhA with the NAD cofactor.
[3] The MM-GBSA binding energy during the 50 – 250 ns range of the MD simulation.

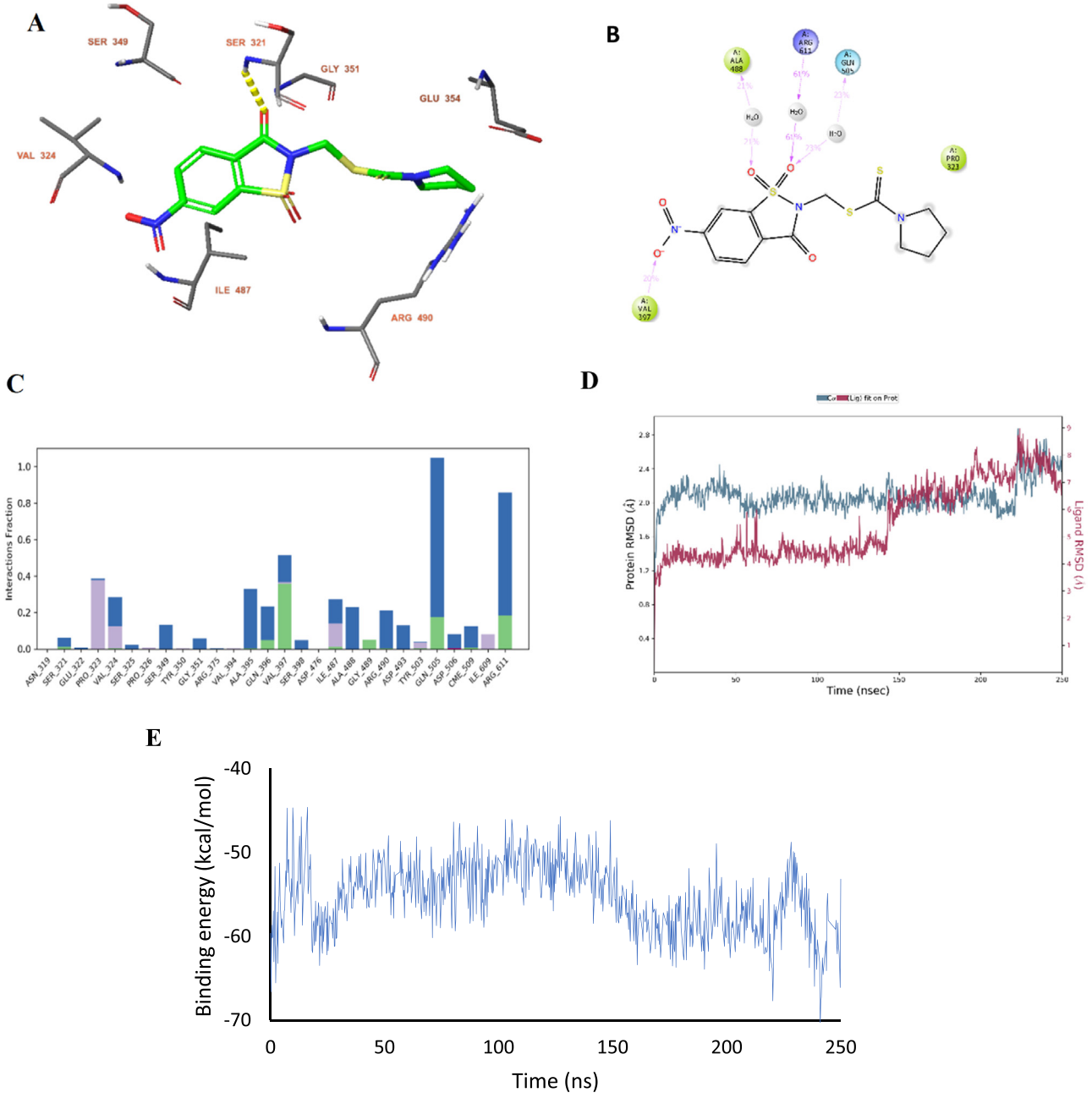

Fig. 4. A) The docked pose of compound **6g** in the active site of FadD32 (5HM3). Hydrogen bonds are indicated in yellow dashed lines. B) The binding interactions during the 250 ns MD simulation. The interactions present for at least 20% of the MD simulation are shown. Hydrophobic amino acids are indicated in green, positively charged amino acids are indicated in purple and polar amino acids are indicted in blue. C) Protein-ligand contacts histogram. Green represents hydrogen bonds, blue represents water-bridged hydrogen bonds, and grey represents hydrophobic interactions. D) RMSD of the protein Cα-atoms (blue) and ligand (red). E) The Protein-ligand interaction energy (kcal/mol) during the MD simulation.

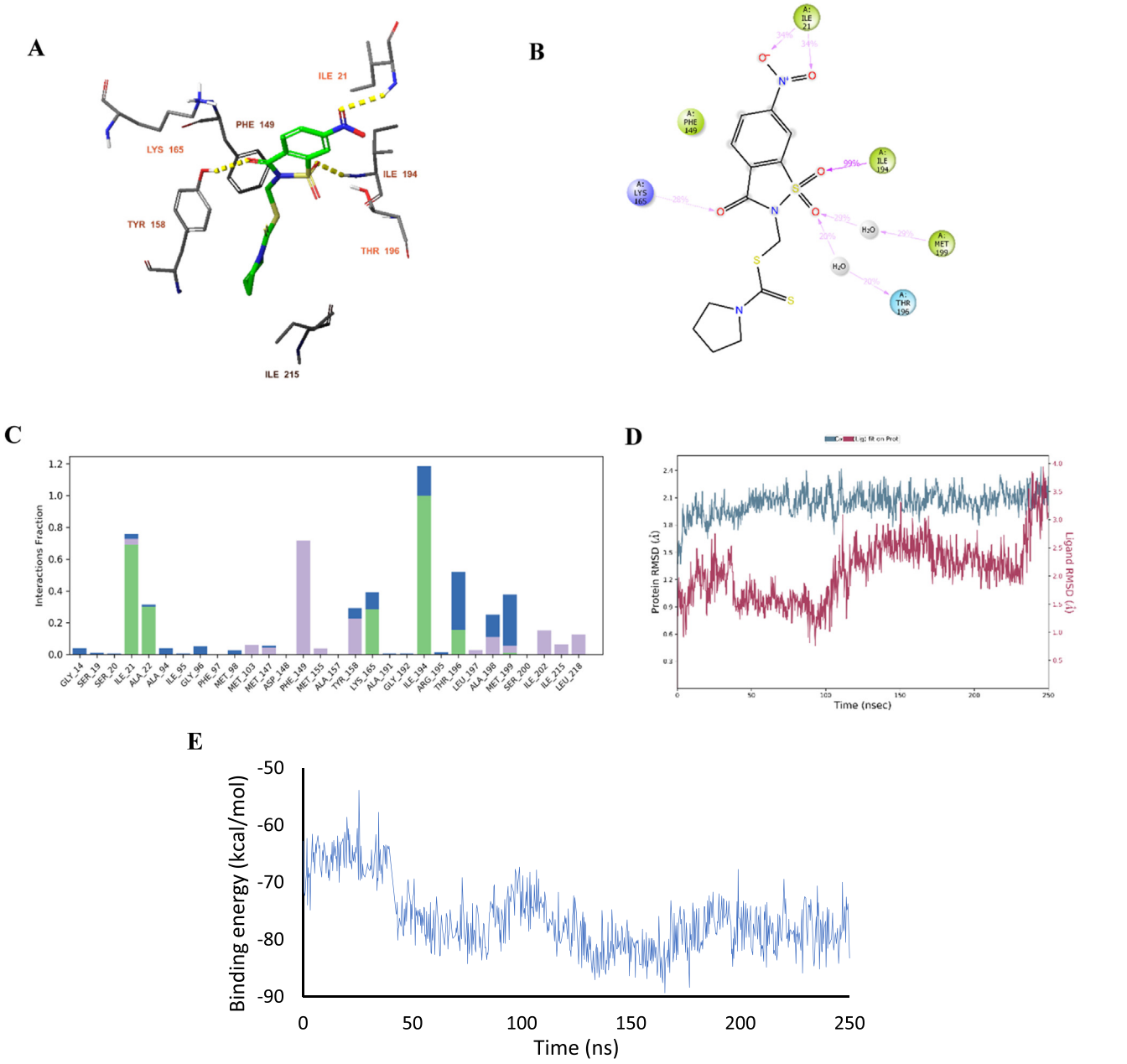

Fig. 5. A) The docked pose of compound **6g** in the active site of InhA (4BGE). Hydrogen bonds are indicated in yellow dashed lines. B) The binding interactions during the 250 ns MD simulation. The interactions present for at least 20% of the MD simulation are shown. Hydrophobic amino acids are indicated in green, positively charged amino acids are indicated in purple and polar amino acids are indicted in blue. C) Protein-ligand contacts histogram. Green represents hydrogen bonds, blue represents water-bridged hydrogen bonds, and grey represents hydrophobic interactions. D) RMSD of the protein Cα-atoms (blue) and ligand (red). E) The Protein-ligand interaction energy (kcal/mol) during the MD simulation.

RMSD value was generally below 3 Å indicating that the docked pose was stable during the simulation. The slight increase of the ligand RMSD in the last 30 ns was due to the large and frequent rotation of the single bonds present in the pyrrolidinedithioate part of the ligand that did not contribute to its binding (Fig. 5D). The average MM-GBSA binding free energy of the InhA-**6g** complex (4BGE) was −76.33 +/- 5.94 kcal/mol. The highest and lowest binding energies were −55 and −90 kcal/mol respectively (Fig. 5E).

The MD simulation of InhA (4BGE) in complex with its cocrystallized ligand indicates that the hydrogen bonds between Tyr158 and Ile194 are maintained throughout the simulation. The RMSD values of the protein Cα-atoms and the ligand were below 3.2 Å. The average MM-GBSA binding free energy was calculated as −94.65 +/- 9.34 kcal/mol. The highest and lowest binding energies were −70 and −130 kcal/mol respectively (See Supplementary, **Fig. S73**).

Pyrrolidine ring has a small distance with Pro156 and Ala157. The introduction of both an electrophilic group and bulky groups cause clashes with Pro156. The nitro group interacts with the protein 34% of the simulation period.

The MM-GBSA binding free energy of InhA-**6g** complex (4TZK) was calculated as −62.10 kcal/mol. The binding pose, however, shows a single π-π interaction with the sidechain of Phe149. In addition, the carbonyl group on the ligand forms a hydrogen bond with the cofactor, NAD, present in the binding site (Fig. 6A). During the 250 ns MD simulation, the π-π interaction between the ligand and the sidechain of Phe149 was maintained almost throughout the simulation (81%). Another π-π interaction was observed

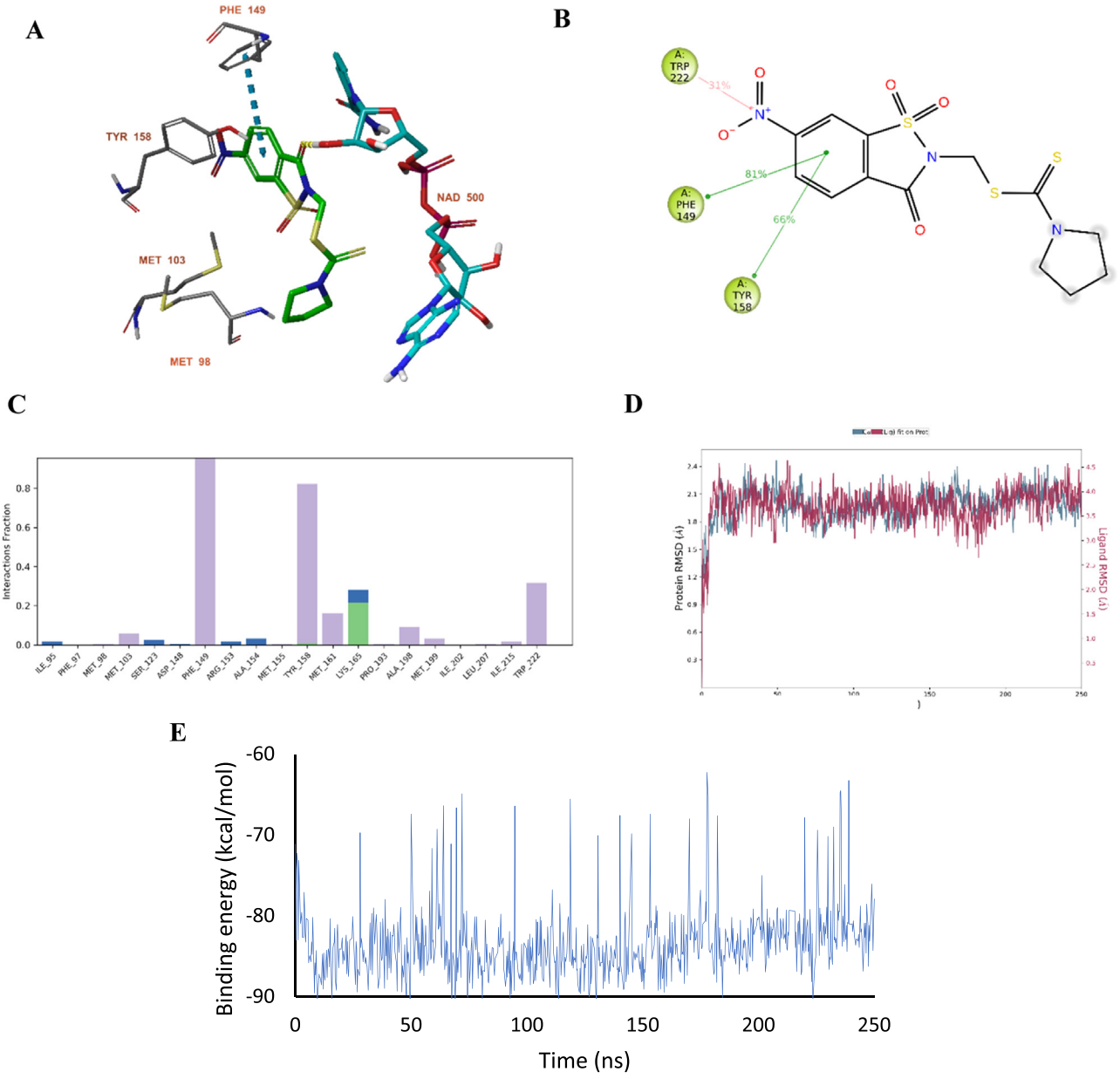

Fig. 6. A) The docked pose of compound **6g** in the active site of InhA (4TZK). Hydrogen bonds are indicated in yellow dashed lines and π-π stackings are indicated in turquoise lines. B) The binding interactions during the 250 ns MD simulation. The interactions present for at least 20% of the MD simulation are shown. Hydrophobic amino acids are indicated in green. C) Protein-ligand contacts histogram. Green represents hydrogen bonds, blue represents water-bridged hydrogen bonds, and grey represents hydrophobic interactions. D) RMSD of the protein Cα-atoms (blue) and ligand (red). E) The Protein-ligand interaction energy (kcal/mol) during the MD simulation.

with the sidechain of Tyr158 which continued for more than 60% of the simulation period (Fig. 6B & C). The RMSD value of the protein Cα-atoms and the ligand is stabilized at 2.1 Å and 4 Å, respectively, indicating that protein conformation and the docked pose were stable (Fig. 6D). The average MM-GBSA binding free energy of the InhA-**6g** complex (4BGE) was −83.55 +/- 4.19 kcal/mol. The highest and lowest binding energies were −60 and −90 kcal/mol respectively (Fig. 6E).

The MD simulation of InhA (4TZK) in complex with its cocrystallized ligand indicates that the hydrogen bond between the ligand and Tyr158 (25%) was not sustained throughout the simulation. The RMSD values of the protein Cα-atoms and the ligand were generally below 2.4 Å. The average MM-GBSA binding free energy was −81,45 +/- 7.14 kcal/mol. The highest and lowest binding energies were −59 and −93 kcal/mol respectively (See Supplementary, **Fig. S74**).

Though the pyrrolidine ring is solvent exposed, it generally moves toward the backbone of Glu96. The insertion of a heteroatom or a bulky group causes clashes with Glu96 (and Phe97). The nitro group interacts with the protein 31% of the simulation period.

The MM-GBSA binding free energy of InhA-**6g** complex (4BII) was calculated as −55.58 kcal/mol. The sulfinyl group and carbonyl group on the nitrosacharrin ring of the ligand formed hydrogen bonds with the sidechain of catalytic residue Tyr158 and Ile194, respectively. The ligand also formed π-π interaction with both the sidechains of Tyr158 and Phe149 (Fig. 7A). Throughout the 250 ns simulation period, the ligand continuously interacted with Tyr158 via either π-π interaction or a water-bridged hydrogen bond. The π-π interaction formed with the sidechain of Phe149 was only maintained for approximately 40% of the simulation time. A hydrophobic interaction was observed with Ile215 for almost 50% of

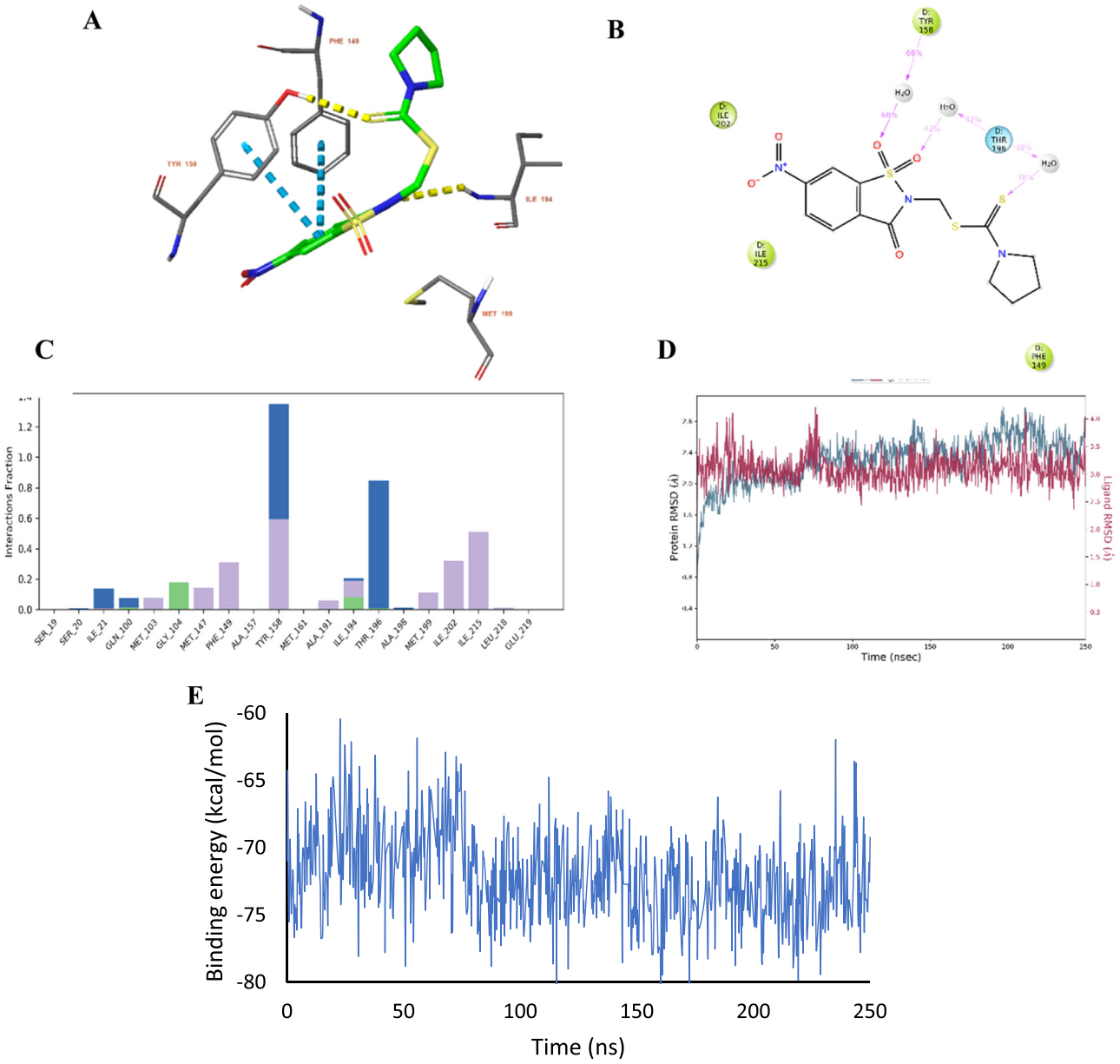

Fig. 7. A) The docked pose of compound **6g** in the active site of InhA (4BII). Hydrogen bonds are indicated in yellow dashed lines and π-π stackings are indicated in turquoise lines. B) The binding interactions during the 250 ns MD simulation. The interactions present for at least 20% of the MD simulation are shown. Hydrophobic amino acids are indicated in green. C) Protein-ligand contacts histogram. Green represents hydrogen bonds, blue represents water-bridged hydrogen bonds, and grey represents hydrophobic interactions. D) RMSD of the protein Cα-atoms (blue) and ligand (red). E) The Protein-ligand interaction energy (kcal/mol) during the MD simulation.

the simulation time. Prior to the simulation, the observed hydrogen bond between the sulfinyl group and Ile194 was not sustained, however, the sulfinyl formed a new water-bridged hydrogen bond with Thr196 and maintained the bond for 40% of the simulation time. In addition, Thr196 equally formed another water-bridged hydrogen bond with the sulfonyl (Fig. 7B & C). The RMSD value of the protein Cα-atoms is generally lower than 2.8 Å indicating that the protein conformation is stable. The ligand RMSD value was generally below 3.5 Å indicating that the docked pose was stable during the simulation (Fig. 7D). The average MM-GBSA binding free energy of the InhA-**6g** complex (4BGE) was −72.08 +/- 3.34 kcal/mol. The highest and lowest binding energies were −60 and −80 kcal/mol respectively (Fig. 7E).

The MD simulation of InhA complex (4BII) in complex with its cocrystallized ligand indicates that the hydrogen bond between the ligand and Tyr158 (28%) was not maintained and either a hydrogen bond or water-bridged hydrogen bond was present with Ile194 throughout the simulation. The RMSD values of the protein Cα-atoms and the ligand were generally below 2.6 Å and 4 Å. The average MM-GBSA binding free energy was −274,27 +/- 15.36 kcal/mol. The highest and lowest binding energies were −220 and −320 kcal/mol, respectively (See Supplementary, **Fig. S75**).

The pyrrolidine ring is positioned in the hydrophobic region of the binding pocket and this reflects the preference of hydrophobic groups. The pyrrolidine frequently forms hydrophobic interactions with Phe149, and Ala191, however, the introduction of bulky and lengthy aliphatic groups causes steric clashes with these amino acid residues.

The InhA-**6g** complex (4D0R) has shown the lowest MM-GBSA binding free energy of −71.61 kcal/mol. The nitrosachharin ring formed a π-π interaction with Phe149 and the nitro group formed

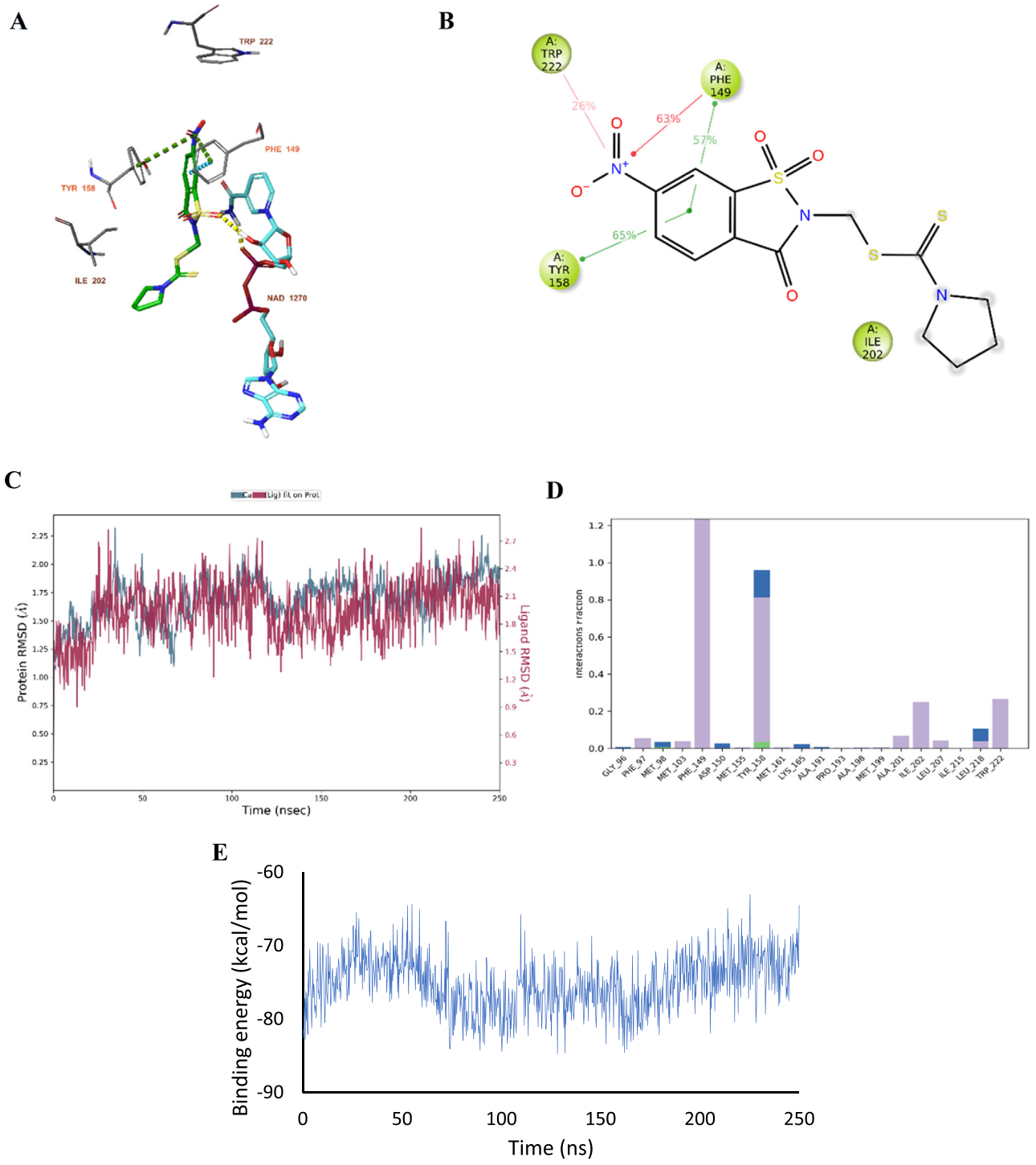

Fig. 8. A) The docked pose of compound **6g** in the active site of InhA (4D0R). Hydrogen bonds are indicated in yellow dashed lines, π-π stackings are indicated in turquoise dashed lines and π-cation interactions are indicated in green dashed lines. B) The binding interactions during the 250 ns MD simulation. The interactions present for at least 20% of the MD simulation are shown. Hydrophobic amino acids are indicated in green. C) Protein-ligand contacts histogram. Green represents hydrogen bonds, blue represents water-bridged hydrogen bonds, and grey represents hydrophobic interactions. D) RMSD of the protein Cα-atoms (blue) and ligand (red). E) The Protein-ligand interaction energy (kcal/mol) during the MD.

π-cation interactions with both Phe149 and Tyr158. In addition, the sulfinyl group on the ligand forms a hydrogen bond with the cofactor, NAD (Fig. 8A). During the 250 ns simulation, the ligand's interaction with Phe149 was sustained throughout the simulation either with π-π (57%) or π-cation (63%) interactions. The π-cation interaction with Tyr158 continued as π-π interaction and was present for 65% of the simulation time. The *in* position of Phe149 enhanced the ligand to frequently interact with both Phe149 and Tyr158. The hydrophobic interaction with Ile202 and n new π-cation interaction formed with Trp222 were present for 26% each (Fig. 8B & C). The RMSD value of the protein Cα-atoms is generally lower than 2.2 Å indicating that the protein conformation is stable. The ligand RMSD value was generally below 2.7 Å indicating that the docked pose was stable during the simulation (Fig. 8D).

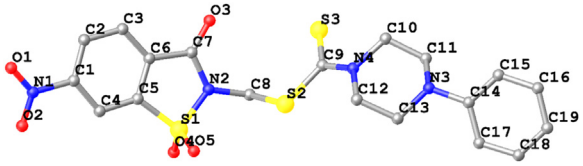

Fig. 9. Thermal ellipsoids with atom labels of compound 6e are drawn at 50% probability. Hydrogen atoms are omitted for clarity.

The average MM-GBSA binding free energy of the InhA-**6g** complex (4D0R) was −75.19 +/- 3.76 kcal/mol. The highest and lowest binding energies were −65 and −84 kcal/mol, respectively (Fig. 8E).

The MD simulation of InhA complex (4D0R) in complex with its cocrystallized ligand indicates that the ligand interacted with Phe149 via π-π interaction (36%) and other hydrophobic contracts during the simulation. The RMSD values of the protein Cα-atoms and the ligand were below 2 Å and 4.5 Å, respectively. The average MM-GBSA binding free energy was −80.26 +/- 7.50 kcal/mol. The highest and lowest binding energies were −60 and −100 kcal/mol respectively (See Supplementary, **Fig. S76**).

The pyrrolidine ring and the backbone of Asp148 are right next to each other. A substitution of an electrophilic group ring causes clashes with Asp148 and the introduction of bulky groups also causes clashes with both the backbone of Asp148 and the side chain of Lys165. The nitro group interacts with the protein for more than half of the simulation period.

2.4. Single crystal X-Ray analyses

Crystals of compound **6e** were obtained from slow evaporation from chloroform and subjected to single X-ray analyses to further elucidate its structure. The molecular structure of compound **6e**, represented in the atom-numbering scheme, is generated with OLEX (v2.1, OlexSys Ltd, Regensburg, Germany) and plotted in Fig. 9. The molecule crystallized in a monoclinic system with P21/c space group. Each unit cell contains 4 independent molecules ($Z = 4$). All the bond distances and bond angles are generally in agreement with similar crystals previously reported [57–59]. The molecule crystallized in a thione form (C = S). The C9—S3 bond lenght is 1.656 (7) Å, which is closer to the average value for C=S (1.681 Å) [60] and shorter than a single C—S bond as in C8—S2 and C9—S2 with bond lengths of 1.804 (6) Å and 1.786 (6) Å, respectively. The thiocarbamate S3—C9—N4 forms a bond angle of 122.9° (4) agrees with the literature [57]. The $S = O$ bond distances (S1—O4/S1—O5) are 1.420 (4) Å and 1.410 (4) Å, respectively, and the bond angle of O4—S1—O5 ($O = S = O$) is 117.4(3) which are all in agreement with the crystals of saccharin derivatives available in the literature [58,59]. The saccharin S1/N2/C1-C7 and the phenyl ring C14-C19 are mostly planar. The piperazine ring displays a chair conformation. Further details on crystal data, data collection, and refinements are included in the supporting information **(Table S77-S82**) and can also be found by downloading CCDC 2209087 via http://www.ccdc.cam.ac.uk/conts/retrieving.html.

3. Conclusion

A series of dithiocarbamates and dithiocarbonates containing a nitrosaccharin group has been successfully prepared via a multistep synthesis, and tested for their antimycobacterial activities. The dithiocarbamates showed generally stronger mycobacterial growth inhibition compared to the dithiocarbonates. Among the dithiocarbamate derivatives, compounds **6d** and **6g** were found to be the most active compounds with IC_{90} values of 0.460 µg/mL and 0.450 µg/mL, respectively. Reverse docking studies in combination with molecular dynamics simulations were performed against nine different potential target proteins of *mycobacterium tuberculosis* to understand the probable mechanism of action of the most active compound **6g**. These studies indicate that compound **6g** may exert its antimycobacterial activity via an interaction mainly with InhA and to a lesser extent with Pks13. Interestingly, compound **6g** was expected to bind to both the apo-form and the NAD-bound form of InhA. Thus, these compounds, and compound **6g** in particular, might be considered potential lead molecules for the development of novel anti-TB medicines.

4. Materials and methods

4.1. Chemical material and apparatus

All chemicals used were obtained from commercial sources. All melting points were measured in open capillary tubes with Buchi 540 and left uncorrected. The progress of the reaction and the purity of the compounds were controlled with TLC on silica gel HF254 (E.Merck, Darmstadt, Germany). Infrared (IR) spectra were recorded as thin KBr pellets on Perkin-Elmer 1600 FTIR spectrophotometer and all values are expressed as υmax cm^{-1}. ^1H NMR, ^{13}C NMR(APT), and HSQC spectra were recorded on a Varian^{UNITY}INOVA 500 MHz and Bruker Avance Neo 500 MHz spectrometers using DMSO–d_6 as a solvent, and chemical shifts are given in ppm with TMS as a Standard. Elemental analysis of all new compounds was performed on a Carlo Erba Model 1106 elemental analyzer. Mass spectral data (APCI+ and ESI+) were recorded on a Waters Alliance HPLC and ZQ micromass (Waters Corporation, Milford, MA, USA), and Agilent 1260 Infinity II LC-MS (Agilent Technologies, Santa Clara, CA, USA) Mass Spectrometer.

4.1.1. Synthesis of 6-nitrosachharin (3)

2-methyl-5-nitrobenzenesulfonamide (**2**) (0.01 mol) prepared as reported in the literature was treated with concentrated H_2SO_4 (12 mL) in a 100 mL beaker. The mixture was heated at 75–80 °C in a steam bath. Chromium (VI) oxide (3 eq) was gently added in small portions until the reaction mixture turned green and viscous. The reaction mixture was further stirred for 10 mins at 65–75–80 °C, cooled in an ice bath, poured into a beaker containing cold water, and eventually stirred to give a crude precipitate of compound **3** which was purified by recrystallizing it from hot ethanol. m.p. 207–208 °C; IR(KBr): υ 1731 (C = O), 1185, 1239 ($S = O$); ^1H NMR (DMSO–d_6/500 MHz): 4.89 (1H, s, NH), 8.04 (d, 1H, J = 8.29 Hz, bzi. C_4-H), 8.55 (dd, 1H, J_1= 8.29, J_2=1.95 Hz, bzi. C_5-H); 8.76 (d, 1H, J = 1.47 Hz, bzi. C_7-H). ^{13}C NMR-HSQC (DMSO–d_6/125 MHz): **8.76, 117.32** [bzi. C_7-H, bzi. C_7]; **8.04, 126.59** [bzi. C_4-H, bzi. C_4]; **8.55, 129.93** [bzi. C_5-H, bzi. C_5]; 134.70 [bzi. C_{3a}]; 142.62 [bzi. C_{7a}]; 151.89 [bzi. C_6]; 161.78 [C = O]. Anal. Calcd for $C_7H_4N_2O_5S$ (216.17): C, 36.85; H, 1.77; N, 12.28; S, 14.05. Found: C, 36.53; H, 1.49; N, 11.93; S, 14.24.

4.1.2. Synthesis of 6-nitro-2-(hydroxymethyl)-1,2-benzisothiazol-3(2H)-on 1,1-dioxide (4)

To a solution of **3** (0.1 mol) in ethanol (100 mL), 37% formaldehyde (70 ml) was added, and the reaction mixture was kept at 0 °C for 16 h. The crude product formed was filtered out and recrystallized from ethanol to afford **4**. m.p. 180–181 °C; IR(KBr): υ 1738 (C = O), 1186, 1241 ($S = O$); ^1H NMR (DMSO–d_6/500 MHz): 5.22 (s, 2H, N–CH_2-), 5.59 (br s, 1H, -OH), 8.36 (d, 1H, J = 8.39 Hz, bzi. C_4-H), 8.73 (dd, 1H, J_1= 8.39, J_2=1.98 Hz, bzi. C_5-H); 9.25 (d, 1H, J = 1.83 Hz, bzi. C_7-H). ^{13}C NMR-APT (DMSO–d_6/125 MHz): 63.90 (N–CH_2-), 118.43 (bzi. C_7), 127.53 (bzi. C_4), 130.71 (bzi. C_5), 131.13 (bzi. C_{3a}), 138.55 (bzi. C_{7a}), 152.29 (bzi. C_6), 157.36 (C = O).]. Anal. Calcd for $C_8H_6N_2O_6S$ (246.20): C, 37.21; H, 2.34; N, 10.85; S, 12.42. Found: C, 37.28; H, 2.52; N, 10.76; S, 12.56.

4.1.3. Synthesis of 6-nitro-2-(chloromethyl)-1,2-benzisothiazol-3(2H)-on 1,1-dioxide (5)

A solution of **4** (0.02 mol) in ether (20 mL) was treated with $SOCl_2$ (40 mL) and kept in an ice bath for 24 h. Excess of $SOCl_2$ was evaporated in vacuo and the obtained residue was recrystallized from acetone to give **5**. m.p. 184–185 °C; IR(KBr): υ 1745 (C = O), 1186, 1244 (*S = O*); ^{1}H NMR (DMSO–d_6/500 MHz): 5.84 (s, 2H, N–CH_2–Cl), 8.40 (s, 1H, bzi. C_4–H), 8.73 (dd, 1H, J_1= 8.30, J_2=1.95 Hz, bzi. C_5–H); 9.34 (d, 1H, *J* = 1.95 Hz, bzi. C_7–H). ^{13}C NMR-HSQC (DMSO–d_6/125 MHz): **9.34, 119.12** [bzi. C_7–H, bzi. C_7]; **8.40, 128.15** [bzi. C_4–H, bzi. C_4]; **8.73, 131.21** [bzi. C_5–H, bzi. C_5]; 135.42 [bzi. C_{3a}]; 143.24 [bzi. C_{7a}]; 152.93 [bzi. C_6]; 156.75 [C = O]. Anal. Calcd for $C_8H_5ClN_2O_5S$ (276.65): C, 34.73; H, 1.82; N, 10.13; S, 11.59. Found: C, 34.98; H, 1.96; N, 10.07; S, 11.30.

4.1.4. General synthesis of (1,1-dioxido-6-nitro-3-oxo-1,2-benzisothiazol-2(3H)-yl)methyl N,N-disubstituted dithiocarbamates (6a-g) / O-alkyl dithiocarbonates (7a-d)

Under reflux, the ethanolic solution of **5** (0.005 mol) was heated for 1 h with *N,N*-disubstituted dithiocarbamate (1 eq) for compounds **6a-g** and O-alkyldithiocarbonate (1 eq) for compounds **7a-d**. The solvent was removed under reduced pressure. The crude residue was washed with H_2O and recrystallized from ethanol.

(1,1-Dioxido-6-nitro-3-oxo-1,2-benzisothiazol-2(3*H*)-yl)methyl *N,N*-methyldithiocarbamate (6a).

Ivory powder, yield 29%; m.p. 107–108 °C; IR(KBr): υ 1737 (C = O), 1236 (C = S), 1185,1266 (*S = O*); ^{1}H NMR (DMSO–d_6/500 MHz): δ 2.40 (s, 6H, 2xCH_3), 5.53 (s, 2H, N–CH_2-S), 8.34 (d, 1H, *J* = 8.29 Hz, bzi. C_4–H), 8.71 (dd, 1H, J_1= 8.79, J_2=1.96 Hz, bzi. C_5–H); 9.29 (d, 1H, *J* = 1.96 Hz, bzi. C_7–H); ^{13}C NMR (APT, DMSO–d_6/125 MHz): 36.62, 36.90 (2xCH_3), 45.16 (N–CH_2-), 118.70 (bzi. C_7), 127.53 (bzi. C_4), 130.84 (bzi. C_5), 130.80 (bzi. C_{3a}), 138.31 (bzi. C_{7a}), 152.52 (bzi. C_6), 157.32 (C = O), 192.09 (C = S). MS-ESI (+): *m/z* 360.3 $[M]^+$. Anal. Calcd for $C_{11}H_{11}N_3O_5S_3$ (361.41): C, 36.56; H, 3.07; N, 11.63; S, 26.62. Found: C, 36.73; H, 3.30; N, 11.39; S, 26.85.

(1,1-Dioxido-6-nitro-3-oxo-1,2-benzisothiazol-2(3*H*)-yl)methyl *N,N*-ethyldithiocarbamate (6b).

Ivory powder, yield 35%; m.p. 141–142 °C; IR(KBr): υ 1735 (C = O), 1236 (C = S), 1185,1266 (*S = O*); ^{1}H NMR (DMSO–d_6/500 MHz): δ 1.19 (t, 6H, *J* = 6.83 Hz, 2xCH_3), 3.72 (q, 2H, *J* = 6.83 Hz, N–CH_2), 3.97 (q, 2H, *J* = 6.83 Hz, N–CH_2), 5.83 (s, 2H, N–CH_2-S), 8.33 (d, 1H, *J* = 8.78 Hz, bzi. C_4–H), 8.70 (ddd, 1H, J_1= 8.29, J_2=1.95, J_3=0.97 Hz, bzi. C_5–H); 9.26 (d, 1H, *J* = 1.95 Hz, bzi. C_7–H). MS-ESI (+): *m/z* 390.0 $[M + H]^+$. Anal. Calcd for $C_{13}H_{15}N_3O_5S_3$ (389.47): C, 40.09; H, 3.88; N, 10.79; S, 24.70. Found: C, 40.21; H, 3.93; N, 10.62; S, 24.57.

(1,1-Dioxido-6-nitro-3-oxo-1,2-benzisothiazol-2(3*H*)-yl)methyl piperidin-1-carbodithioate (6c).

Ivory powder, yield 27%; m.p. 143–144 °C; IR(KBr): υ 1745 (C = O), 1241 (C = S), 1186, 1260 (*S = O*); ^{1}H NMR (DMSO–d_6/500 MHz): δ 1.60–1.67 (m, 6H, piperidine $C_{3,4,5}$–H), 4.16 (br s, 4H, piperidine $C_{2,6}$–H.), 5.84 (s, 2H, N–CH_2-S), 8.33 (d, 1H, *J* = 7.31 Hz, bzi. C_4–H), 8.70 (dd, 1H, J_1= 7.31, J_2=1.95 Hz, bzi. C_5–H); 9.26 (d, 1H, *J* = 1.95 Hz, bzi. C_7–H); ^{13}C NMR (HSQC, DMSO–d_6/125 MHz): δ **1.60–1.67, 24.12** [piperidine $C_{3,4,5}$–H, piperidine $C_{3,5}$]; **1.60–1.67, 25.89** [piperidine $C_{3,4,5}$–H, piperidine C_4]; **5.84, 45.76** [N–CH_2-]; **4.16, 52.78** [piperidine C_2–H, piperidine C_2]; **4.16, 55.87** [piperidine C_6–H, piperidine C_6]; **9.26, 118.86** [bzi. C_7–H, bzi. C_7]; **8.33, 127.76** [bzi. C_4–H, bzi. C_4]; **8.70, 131.02** [bzi. C_5–H, bzi. C_5]; 131.04 [bzi. C_{3a}]; 139.99 [bzi. C_{7a}]; 152.74 [bzi. C_6]; 157.52 [C = O]; 191.39 [C = S]. MS-ESI (+): *m/z* 402.0 $[M + H]^+$. Anal. Calcd for $C_{14}H_{15}N_3O_5S_3$ (401.48): C, 41.88; H, 3.77; N, 10.47; S, 23.96. Found: C, 41.80; H, 3.58; N, 10.53; S, 23.79.

(1,1-Dioxido-6-nitro-3-oxo-1,2-benzisothiazol-2(3*H*)-yl)methyl 3-methylpiperidin-1-carbodithioate (6d).

Light yellow powder, yield 36%; m.p. 121–122 °C; IR(KBr): υ 1725 (C = O), 1231 (C = S), 1188,1264 (*S = O*); ^{1}H NMR (DMSO–d_6/500 MHz): δ 0.88 (s, 3H, piperidine CH_3), 1.24–1.34 (m, 1H, piperidine C_4–$H_{ax.}$), 1.43–1.49 (m, 1H, piperidine C_5–$H_{ax.}$), 1.71–1.79 (m, 3H, C_3–H, $C_{4,5}$–H_{eq}), 3.06, 3.15 (2t, 1H, *J* = 12.20 Hz, piperidine C_2–$H_{ax.}$), 3.37 (d, 1H, *J* = 10.74 Hz, piperidine C_6–$H_{ax.}$), 4.20, 4.29 (2d, 1H, *J* = 13.18 Hz, piperidine C_2–$H_{eq.}$), 5.03 (br s, 1H, piperidine C_6–$H_{eq.}$), 5.84 (s, 2H, N–CH_2-S), 8.34 (d, 1H, *J* = 8.29 Hz, bzi. C_4–H), 8.70 (dd, 1H, J_1= 8.29, J_2=1.95, bzi. C_5–H); 9.26 (d, 1H, *J* = 1.95 Hz, bzi. C_7–H). MS-ESI (+): *m/z* 415.9 $[M + H]^+$. Anal. Calcd for $C_{15}H_{17}N_3O_5S_3$ (415.50): C, 43.36; H, 4.12; N, 10.11; S, 23.15. Found: C, 43.52; H, 4.19; N, 10.04; S, 23.36.

(1,1-Dioxido-6-nitro-3-oxo-1,2-benzisothiazol-2(3*H*)-yl)methyl 4-phenylpiperazin-1-carbodithioate (6e).

Yellow powder, yield 40%; m.p. 178–179 °C; IR(KBr): υ 1746 (C = O), 1226 (C = S), 1182,1272 (*S = O*); ^{1}H NMR (DMSO–d_6/500 MHz): δ 4.05 (br s, 4H, piperazine $C_{3,5}$–H), 4.37 (d, 4H, *J* = 14.64 Hz, piperazine $C_{2,6}$–H), 5.87 (s, 2H, N–CH_2-S), 6.80 (t, 1H, *J* = 7.32 Hz, phenyl C_4–H), 6.92 (d, 2H, *J* = 8.30 Hz, phenyl $C_{2,6}$–H), 7.21 (t, 2H, *J* = 8.30 Hz, phenyl $C_{3,5}$–H), 8.34 (d, 1H, *J* = 8.78 Hz, bzi. C_4–H), 8.70 (dd, 1H, J_1= 8.29, J_2=1.95 Hz, bzi. C_5–H), 9.27 (d, 1H, *J* = 1.95 Hz, bzi. C_7–H). ^{13}C NMR (HSQC, DMSO–d_6/125 MHz): δ **5.87, 45.58** [N–CH_2-S]; **4.05, 50.51** [piperazine $C_{3,5}$–H, piperazine $C_{3,5}$]; **4.37, 51.95** [piperazine $C_{2,6}$–H, piperazine $C_{2,6}$]; **6.92, 116.16** [phenyl $C_{2,6}$–H, phenyl $C_{2,6}$]; **9.27, 118.90** [bzi. C_7–H, bzi. C_7]; **6.80, 120.01** [phenyl C_4–H, phenyl C_4]; **8.34, 127.78** [bzi. C_4–H, bzi. C_4]; **7.21, 129.74** [phenyl $C_{3,5}$–H, phenyl $C_{3,5}$]; **8.70, 131.04** [bzi. C_5–H, bzi. C_5]; 131.05 [bzi. C_{3a}]; 138.57 [bzi. C_{7a}]; 150.64 [phenyl C_1]; 152.75 [bzi. C_6]; 157.54 [C = O]; 192.18 [C = S]. MS-ESI (+): *m/z* 479.0 $[M + H]^+$. Anal. Calcd for $C_{19}H_{18}N_4O_5S_3$ (478.57): C, 47.68; H, 3.79; N, 11.71; S, 20.10. Found: C, 47.46; H, 3.52; N, 11.79; S, 20.31.

(1,1-Dioxido-6-nitro-3-oxo-1,2-benzisothiazol-2(3*H*)-yl)methyl 2,6-dimethylmorpholin-4-carbodithioate (6f).

Yellow powder, yield 55%; m.p. 194–195 °C; IR(KBr): υ 1727 (C = O), 1233 (C = S) 1185,1264 (*S = O*); ^{1}H NMR (DMSO–d_6/500 MHz): δ 1.15 (d, 6H, *J* = 1.46 Hz, 2xCH_3), 2.90 (t, 1H, *J* = 11.44 Hz, morpholine C_3–$H_{ax.}$), 3.06 (t, 1H, *J* = 11.44 Hz, morpholine C_5–$H_{ax.}$), 3.59 (br s, 2H, morpholine $C_{2,6}$–H), 4.35 (dd, 1H, J_1=9.31, J_2=4.27 Hz, morpholine C_5–$H_{eq.}$), 5.23 (d, 1H, *J* = 13.58 Hz, morpholine C_3–$H_{eq.}$), 5.87 (s, 2H, N–CH_2-S), 8.36 (d, 1H, *J* = 8.39 Hz, bzi. C_4–H), 8.73 (dd, 1H, J_1= 8.39, J_2=1.98 Hz, bzi. C_5–H), 9.30 (d, 1H, *J* = 1.83 Hz, bzi. C_7–H). ^{13}C NMR (APT, DMSO–d_6/125 MHz): 18.61, 18.90 (2xCH_3), 45.16 (N–CH_2-), 55.53 (morpholine C_5), 56.76 (morpholine C_3), 71.29 (morpholine $C_{2,6}$), 118.70 (bzi. C_7), 127.53 (bzi. C_4), 130.84 (bzi. C_5), 130.80 (bzi. C_{3a}), 138.31 (bzi. C_{7a}), 152.52 (bzi. C_6), 157.32 (C = O), 192.09 (C = S). ^{13}C NMR (HSQC, DMSO–d_6/125 MHz): δ **1.15; 18.61, 18.90** [CH_3]; **3.06, 4.36; 55.53** [morpholine C_5–$H_{ax.}$; morpholine C_5–$H_{eq.}$; morpholine C_5]; **2.90, 5.20; 56.76** [morpholine C_3–$H_{ax.}$; morpholine C_3–$H_{eq.}$; morpholine C_3]; 5.87, 45.16 [N–CH_2-]; **9.30, 118.70** [bzi. C_7–H, bzi. C_7]; **8.36, 127.53** [bzi. C_4–H, bzi. C_4]; **8.73, 130.84** [bzi. C_5–H, bzi. C_5]. MS-ESI (+): *m/z* 432,38 $[M + H]^+$. Anal. Calcd for $C_{15}H_{17}N_3O_6S_3$ (431.50): C, 41.75; H, 3.97; N, 9.74; S, 22.29. Found: C, 41.87; H, 4.01; N, 9.58; S, 22.41.

(1,1-Dioxido-6-nitro-3-oxo-1,2-benzisothiazol-2(3*H*)-yl)methyl pyrrolidin-1-carbodithioate (6g**).**

Ivory powder, yield 70%; m.p. 226–7 °C; IR(KBr): υ 1743 (C = O), 1211 (C = S), 1183, 1265 (*S = O*); ^{1}H NMR (DMSO–d_6/500 MHz): δ 1.93 (2H, p, *J* = 6.87 Hz, pyrrolidine C_3–H), 2.02 (2H, p, *J* = 6.71 Hz, pyrrolidine C_4–H), 3.64 (2H, t, *J* = 6.87 Hz, pyrrolidine C_2–H), 3.82 (2H, t, *J* = 6.87 Hz, pyrrolidine C_5–H), 5.85 (2H, s, CH_2), 8.35 (1H, d, *J* = 8.39 Hz, C_4–H), 8.73 (1H, dd, *J* = 8.39, 1.98 Hz, C_5–H), 9.30 (1H, d, *J* = 1.98 Hz, C_7–H). ^{13}C NMR (APT, DMSO–d_6/125 MHz): 24.13 (pyrrolidine C_3), 25.97 (pyrrolidine C_4), 44.75 (N–CH_2-), 51.14 (pyrrolidine C_2), 55.97 (pyrrolidine

C_5), 118.68 (bzi. C_7), 127.52 (bzi. C_4), 130.81 (bzi. C_5), 138.34 (bzi. C_{7a}), 152.74 (bzi. C_6), 157.39 (C = O), 187.66 (C = S). MS-APCI (+): *m/z* 388.50 $[M + H]^+$. Anal. Calcd for $C_{13}H_{13}N_3O_5S_3$ (387.454): C, 40.30; H, 3.38; N, 10.85; S, 24.83. Found: C, 40.21; H, 3.51; N, 10.74; S, 24.93.

(1,1-Dioxido-6-nitro-3-oxo-1,2-benzisothiazol-2(3*H*)-yl)methyl O-ethyl dithiocarbonate (7a).

Yellow powder, yield 65%; m.p. 111–112 °C; IR(KBr): υ 1737 (C = O), 1235 (C = S), 1185,1265 (*S = O*); ^{1}H NMR (DMSO–d_6/500 MHz): δ 1.45 (t, 3H, *J* = 7.17 Hz, ethyl CH_3), 4.71 (q, 2H, *J* = 7.17 Hz, O–CH_2), 5.55 (s, 2H, N–CH_2-S), 8.36 (d, 1H, *J* = 8.39 Hz, bzi. C_4-H), 8.74 (dd, 1H, J_1= 8.39, J_2=1.98 Hz, bzi. C_5-H), 9.32 (d, 1H, *J* = 2.44 Hz, bzi. C_7-H). ^{13}C NMR (APT, DMSO–d_6/125 MHz): 13.81 (CH_3), 42.62 (N–CH_2-), 71.75 (O–CH_2), 118.69 (bzi. C_7), 127.59 (bzi. C_4), 130.85 (bzi. C_5), 138.20 (bzi. C_{7a}), 152.51 (bzi. C_6), 157.12 (C = O), 209.71 (C = S). MS-APCI (+): *m/z* 165.80. Anal. Calcd for $C_{11}H_{10}N_2O_6S_3$ (362.40): C, 36.46; H, 2.78; N, 7.73; S, 26.54. Found: C, 36.50; H, 2.69; N, 7.71; S, 26.69.

(1,1-Dioxido-6-nitro-3-oxo-1,2-benzisothiazol-2(3*H*)-yl)methyl O-propyl dithiocarbonate (7b).

Ivory flakes, yield 60%; m.p. 71–72 °C; IR(KBr): υ 1737 (C = O), 1238 (C = S), 1184, 1265 (*S = O*); ^{1}H NMR (DMSO–d_6/500 MHz): δ 0.99 (t, 3H, *J* = 7.32 Hz, propyl CH_3), 1.86 (hex., 2H, *J* = 7.32 Hz, propyl -CH_2-), 4.62 (t, 2H, *J* = 6.71 Hz, O–CH_2), 5.55 (s, 2H, N–CH_2-S), 8.36 (d, 1H, *J* = 8.39 Hz, bzi. C_4-H), 8.73 (dd, 1H, J_1= 8.39, J_2=1.98 Hz, bzi. C_5-H), 9.33 (d, 1H, *J* = 1.98 Hz, bzi. C_7-H). ^{13}C NMR (APT, DMSO–d_6/125 MHz): 10.66 (CH_3), 21.43 (-CH_2-), 42.57 (N–CH_2-), 77.01 (O–CH_2), 118.72 (bzi. C_7), 127.60 (bzi. C_4), 130.87 (bzi. C_5), 130.89 (bzi. C_{3a}), 138.19 (bzi. C_{7a}), 152.52 (bzi. C_6), 157.13 (C = O), 209.88 (C = S). MS-APCI (+): *m/z* 165.73. Anal. Calcd for $C_{12}H_{12}N_2O_6S_3$ (376.42): C, 38.29; H, 3.21; N, 7.44; S, 25.55. Found: C, 38.25; H, 3.24; N, 7.51; S, 25.47.

(1,1-Dioxido-6-nitro-3-oxo-1,2-benzisothiazol-2(3*H*)-yl)methyl O-pentyl dithiocarbonate (7c).

Yellow flakes, yield 65%; m.p. 62–63 °C; IR(KBr): υ 1739 (C = O), 1238 (C = S), 1183, 1259 (*S = O*); ^{1}H NMR (DMSO–d_6/500 MHz): δ 0.89 (t, 3H, *J* = 7.17 Hz, pentyl CH_3), 1.30–1.42 (m, 4H, $OCH_2CH_2CH_2CH_2CH_3$), 1.85 (2H, *J* = 6.87 Hz, $OCH_2CH_2CH_2CH_2CH_3$), 4.66 (t, 2H, *J* = 6.56 Hz, O–CH_2), 5.55 (s, 2H, N–CH_2-S), 8.36 (d, 1H, *J* = 8.39 Hz, bzi. C_4-H), 8.74 (dd, 1H, J_1= 8.39, J_2=1.98 Hz, bzi. C_5-H), 9.33 (d, 1H, *J* = 1.83 Hz, bzi. C_7-H). ^{13}C NMR (APT, DMSO–d_6/125 MHz): 14.25 (CH_3), 22.23 (pentyl C_4-H), 27.58 (pentyl C_3-H), 27.88 (pentyl C_2-H), 42.57 (N–CH_2-), 75.57 (O–CH_2), 118.73 (bzi. C_7), 127.59 (bzi. C_4), 130.86 (bzi. C_5), 130.88 (bzi. C_{3a}), 138.19 (bzi. C_{7a}), 152.50 (bzi. C_6), 157.12 (C = O), 209.83 (C = S). MS-APCI (+): *m/z* 165.24. Anal. Calcd for $C_{14}H_{16}N_2O_6S_3$ (404.48): C, 41.57; H, 3.99; N, 6.93; S, 23.78. Found: C, 41.61; H, 4.03; N, 6.98; S, 23.67.

(1,1-Dioxido-6-nitro-3-oxo-1,2-benzisothiazol-2(3*H*)-yl)methyl O-cyclopentyl dithiocarbonate (7d).

Ivory powder, yield 68%; m.p. 100–101 °C; IR(KBr): υ 1747 (C = O), 1238 (C = S), 1188,1267 (*S = O*); ^{1}H NMR (DMSO–d_6/500 MHz): δ 1.61–1.63 (m, 2H, cyclopentyl $C_{3,4}$-$H_{ax.}$), 1.76–1.78 (m, 2H, cyclopentyl $C_{3,4}$-$H_{eq.}$), 1.94–1.98 (m, 4H, cyclopentyl $C_{2,5}$-H), 5.48 (s, 2H, N–CH_2-S), 5.84–5.85 (m, 1H, cyclopentyl C_1-H), 8.34 (d, 1H, *J* = 8.30 Hz, bzi. C_4-H), 8.70 (dd, 1H, J_1= 8.30, J_2=1.95, bzi. C_5-H), 9.30 (d, 1H, *J* = 1.95 Hz, bzi. C_7-H); ^{13}C NMR (HSQC, DMSO–d_6/125 MHz): δ **1.61–1.63; 1.76–1.78; 24.28** [cyclopentyl $C_{3,4}$-H_{ax}; cyclopentyl $C_{3,4}$-$H_{eq.}$; cyclopentyl $C_{3,4}$]; **1.94–1.98, 32.65** [cyclopentyl $C_{2,5}$-H cyclopentyl $C_{2,5}$]; **5.48, 42.44** [N–CH_2-S]; **5.84–5.85, 89.63** [cyclopentyl C_1-H, cyclopentyl C_1]; **9.30, 118.94** [bzi. C_7-H, bzi. C_7]; **8.34, 127.81** [bzi. C_4-H, bzi. C_4]; **8.70, 131.09** [bzi. C_5-H, bzi. C_5]; 138.44 [bzi. C_{7a}]; 152.76 [bzi. C_6]; 157.32 [C = O]; 208.87 [C = S]. MS-ESI (+): *m/z* 424.9 $[M+Na]^+$. Anal. Calcd for $C_{14}H_{14}N_2O_6S_3$ (402.46): C, 41.78; H, 3.51; N, 6.96; S, 23.90. Found: C, 41.81; H, 3.59; N, 6.92; S, 23.85.

4.2. Biological activity

Microplate Alamar Blue Assay (MABA)

Antimicrobial susceptibility testing was performed in black, clear-bottomed, 96-well microplates (black view plates; Packard Instrument Company, Meriden, Conn.) to minimize background fluorescence. Outer perimeter wells were filled with sterile water to prevent dehydration in experimental wells. Initial drug dilutions were prepared in either dimethyl sulfoxide or distilled deionized water, and subsequent twofold dilutions were performed in 0.1 mL of 7H9GC (no Tween 80) in the microplates. BACTEC 12B-passaged inocula were initially diluted 1:2 in 7H9GC, and 0.1 mL was added to wells. The determination of bacterial titer yielded 1×10^6 CFU/ml in plate well for H_{37}Rv. Frozen inocula were initially diluted at 1:20 in BACTEC 12B medium followed by a 1:50 dilution in 7H9GC. The addition of 1/10 mL to wells resulted in a final bacterial titer of 20×10^5 CFU/ml for H_{37}Rv. Wells containing drugs only were used to detect autofluorescence of compounds. Additional control wells consisted of bacteria only (B) and medium only (M). Plates were incubated at 37 °C. Starting on day 4 of incubation, 20 μL of 10x alamarBlue solution (Alamar Biosciences/Accumed, Westlake, Ohio) and 12.5 μL of 20% Tween 80 were added to one B well and one M well, and plates were reincubated at 37 °C. Wells were observed 12 and 24 h later for a color change from blue to pink and a reading of ≥50,000 fluorescence units (FU). Fluorescence was measured in a Cytofluor II microplate fluorometer (PerSeptive Biosystems, Framingham, Mass.) in bottom-reading mode with excitation at 530 nm and emission at 590 nm. If the B wells become pink after 24 h, the reagent is added to the entire plate. If the well remains blue or ≥50,000 FU is measured, additional M and B wells are tested daily until a color change occurred, at which time reagents are added to all remaining wells. Plates were then incubated at 37 °C, and results were recorded at 24 h post-reagent addition. Visual MICs were defined as the lowest concentration of drug that prevented a color change. For fluorometric MICs, background subtraction was performed on all wells with a mean of triplicate M wells. Percent inhibition was defined as (1 – (test well FU/mean FU of triplicate B wells) x 100). The lowest drug concentration effecting an inhibition of ≥90% was considered the MIC.

4.3. Single crystal X-Ray instrumentation

Single crystals of compound **6e** ($C_{19}H_{18}N_4O_5S_3$) were obtained by from slow evaporation. A suitable crystal was then selected, mounted on a micromount, and attached to a goniometer head on a Bruker D8 VENTURE diffractometer. The crystal was kept at room temperature (296.27 K) during data collection. Using Olex2 [61], the structure was solved with the SHELXS-1997 [62] structure solution program using direct methods and refined with the Olex2.refine [63] refinement package using Levenberg-Marquardt minimization. A highly disordered solvent (water) molecule was masked using Squeeze software [64].

4.4. Molecular modeling studies

The Schrödinger software package (v2021–2, Schrödinger, Inc., New York) was used for the modeling studies.

Preparation of Protein Structures

Selected crystal structures were downloaded from the Protein Data Bank. Chain A of each structure was retained and the rest of the chains with the water molecules were deleted except for 4BII, where chain D was retained instead of chain A. The Protein Preparation Wizard module was used to prepare the remaining protein structures, which were pre-processed by adding hydrogens

and missing side chains if present. The N- and C-terminals of the proteins were capped and subsequently, the system was minimized using the OPLS4 force field.

Receptor Grid Generation

A grid file was generated using the Receptor Grid Generation tool. The grid was prepared around the centroid of the cocrystallized ligand. All hydroxyl groups of the Ser, Thr-and Tyr-residues that were lining the binding pocket were allowed to rotate during dockings.

Reverse Virtual Screening

First, the docking protocols were validated by successfully re-docking the reference ligands into the active site of the selected crystal structures using high throughput virtual screening (HTVS) protocol and flexible ligand sampling. The default scaling factor of 0.8 and partial charge cutoff of 0.15 for van der Waals radii were maintained. The planarity of conjugated π groups was enhanced and Epik state penalties for docking were used. Using the Virtual Screening Workflow module and the prepared grids, the ligand was sequentially docked with the HTVS scoring function (5 poses per ligand retained) and subsequently rescored with the Standard Precision (SP) and Extra Precision (XP) scoring functions. Finally, only the highest scoring docked pose (XP) was retained and energy minimized and rescored with MM-GBSA. All binding pocket amino acids within 5 Å from the ligand were included in the minimization.

Molecular Dynamics Simulations

All molecular dynamics simulations were performed using the Desmond tool. The selected docked poses (ligand-enzyme complexes) were initially placed at the center of an orthorhombic box with periodic boundary conditions (minimal distance of 10 Å between protein and boundary). Afterward, both water molecules (Tip5p) and counter ions (NaCl; 0.15 M) were added to generate a solvated and neutral system. The system was energy minimized for 100 ps (OPLS4) with position restraints on all protein and ligand atoms. Finally, the system was simulated for 250 ns at constant temperature (300 K, Nose-Hoover Chain, default values) and pressure (1 bar, Martyna-Tobias-Klein, default values) using the RESPA integrator and without any position restrains. The time step was set to 0.002 fs. Root Mean Square Deviation (RMSD) of the protein Cα-atoms and the interactions between the ligand and the protein obtained during the 250 ns MD simulation were analyzed from simulated trajectories using the Simulation Interaction Diagram tool. The MM-GBSA binding free energies of the complexes during the 250 ns simulation period were calculated using the *thermal_MMGBSA.py* script [65].

Credit author statement

Muhammed Trawally: Writing – original draft. **Kübra Demir-Yazıcı:** Writing – original draft. **Serap İpek Dingiş-Birgül:** Writing – original draft. **Kerem Kaya:** Conducting Single crystal X-ray studies. **Atilla Akdemir:** Conceptualization, Writing – review & editing, Writing – original draft. **Özlen Güzel-Akdemir:** Conceptualization, Writing – review & editing, Supervision, Project administration, Funding acquisition, Writing – original draft.

Declaration of Competing Interest

The authors declare that they have no known competing financial interests or personal relationships that could have appeared to influence the work reported in this paper.

Data availability

Data will be made available on request.

Acknowledgments

Antimycobacterial data were provided by the Tuberculosis Antimicrobial Acquisition and Coordinating Facility (TAACF) through a research and development contract with the U.S. National Institute of Allergy and Infectious Diseases. Thanks are addressed to Dr. Joseph A. Maddry (TAACF) and his team for their collaboration.

Funding

This work was supported by the Research Fund of Istanbul University (Project number 544/05052006).

Supplementary materials

Supplementary material associated with this article can be found, in the online version, at doi:10.1016/j.molstruc.2022.134818.

References

[1] G.T. ProgrammeGlobal Tuberculosis Report 2021, World Health Organization, 14 October 2021.
[2] K. Zaman, Tuberculosis: a global health problem, J. Health Popul. Nutr. 28 (2010) 111–113, doi:10.3329/jhpn.v28i2.4879.
[3] T.K. Burki, The global cost of tuberculosis, Lancet Respirat. Med. 6 (2018) 13, doi:10.1016/S2213-2600(17)30468-X.
[4] D.R. Silva, M. Fernanda Carvalho de Queiroz, G.B. Migliori, Shortened tuberculosis treatment regimens: what is new? Jornal Brasileiro de Pneumologia 46 (2020) e20200009, doi:10.36416/1806-3756/e20200009.
[5] S. Silva, N. Arinaminpathy, R. Atun, E. Goosby, M. Reid, Economic impact of tuberculosis mortality in 120 countries and the cost of not achieving the Sustainable Development Goals tuberculosis targets: a full-income analysis, Lancet Glob. Health 9 (2021) e1372–e1379, doi:10.1016/S2214-109X(21)00299-0.
[6] A. Zumla, P. Nahid, S.T. Cole, Advances in the development of new tuberculosis drugs and treatment regimens, Nat. Rev. Drug Discov. 12 (2013) 388–404, doi:10.1038/nrd4001.
[7] R. Prasad, Multidrug and extensively drug-resistant TB (M/XDR-TB): problems and solutions, Indian J. Tuberc. 57 (2010) 180–191.
[8] E. Ashry, E. Sayed H, M.R. Amer, O.M. Abdalla, A.A. Aly, S. Soomro, A. Jabeen, S.A. Halim, M. Ahmed Mesaik, Z. Ul-Haq, Synthesis, biological evaluation, and molecular docking studies of benzyl, alkyl and glycosyl 2-(arylamino)-4,4-dimethyl-6-oxo-cyclohex-1-enecarbodithioates, as potential immunomodulatory and immunosuppressive agents, Bioorg. Med. Chem. 20 (2012) 3000–3008, doi:10.1016/j.bmc.2012.03.003.
[9] S. Fayyaz, F. Shaheen, S. Ali, S. Naseer, S. Rosario, Structural elucidation and antibacterial activity of new dialkylstannyl- and chlorodialkylstannyl(IV) 3,4-dihydroisoquinoline-2-(1H)-carbodithioate, J. Mol. Struct. 1244 (2021) 131213, doi:10.1016/j.molstruc.2021.131213.
[10] S.D. Shinde, A.P. Sakla, N. Shankaraiah, An insight into medicinal attributes of dithiocarbamates: bird's eye view, Bioorg. Chem. 105 (2020) 104346, doi:10.1016/j.bioorg.2020.104346.
[11] D. Chaturvedi, S. Zaidi, A.K. Chaturvedi, S. Vaid, A.K. Saxena, An efficient protocol for the synthesis of β-substituted ethyl dithiocarbamates: a novel class of anti-cancer agents, 0975–0983 (2016).
[12] J.W.de F. Oliveira, H.A.O. Rocha, W.M.T.Q. de Medeiros, M.S. Silva, Application of dithiocarbamates as potential new antitrypanosomatids-drugs: approach chemistry, functional and biological, Molecules (2019) 24, doi:10.3390/molecules24152806.
[13] O. Güzel, A. Salman, Synthesis, antimycobacterial and antitumor activities of new (1,1-dioxido-3-oxo-1,2-benzisothiazol-2(3H)-yl)methyl N,N-disubstituted dithiocarbamate/O-alkyldithiocarbonate derivatives, Bioorg. Med. Chem. 14 (2006) 7804–7815, doi:10.1016/j.bmc.2006.07.065.
[14] E.N. Esfahani, M. Mohammadi-Khanaposhtani, Z. Rezaei, Y. Valizadeh, R. Rajabnia, M. Hassankalhori, F. Bandarian, M.A. Faramarzi, N. Samadi, M.R. Amini, M. Mahdavi, B. Larijani, New ciprofloxacin–dithiocarbamate–benzyl hybrids: design, synthesis, antibacterial evaluation, and molecular modeling studies, Res. Chem. Intermed. 45 (2019) 223–236, doi:10.1007/s11164-018-3598-3.
[15] M.-.S. Kang, E.-.K. Choi, D.-.H. Choi, S.-.Y. Ryu, H.-.H. Lee, H.-.C. Kang, J.-.T. Koh, O.-.S. Kim, Y.-.C. Hwang, S.-.J. Yoon, S.-.M. Kim, K.-.H. Yang, I.-.C. Kang, Antibacterial activity of pyrrolidine dithiocarbamate, FEMS Microbiol. Lett. 280 (2008) 250–254, doi:10.1111/j.1574-6968.2008.01069.x.
[16] U. MOHSEN, Synthesis and Antimicrobial Activity of Some Piperazine Dithiocarbamate Derivatives, Turk. J. Pharmaceut. Sci. 11 (2014) 347–354.
[17] E. Ghabraie, H. Moghimi, S. Balalaie, M. Bararjanian, F. Rominger, H.R. Bijanzadeh, Efficient synthesis of functionalized dithiocarbamate derivatives through one-pot three-component reaction and evaluation of their antimicrobial activities, J. Iran. Chem. Soc. 10 (2013) 725–732, doi:10.1007/s13738-012-0206-0.
[18] G.-.K. Nalan, Synthesis and biological activity of thiazole dithiocarbamate derivatives, Lett. Drug Des. Discovery 11 (2014) 814–823.

[19] S.M. Mamba, A.K. Mishra, B.B. Mamba, P.B. Njobeh, M.F. Dutton, E. Fosso-Kankeu, Spectral, thermal and in vitro antimicrobial studies of cyclohexylamine-N-dithiocarbamate transition metal complexes, Spectrochim. Acta A Mol. Biomol. Spectrosc. 77 (2010) 579–587, doi:10.1016/j.saa.2010.06.002.

[20] D.S. Pal, D.K. Mondal, R. Datta, Identification of metal dithiocarbamates as a novel class of antileishmanial agents, Antimicrob. Agents Chemother. 59 (2015) 2144–2152, doi:10.1128/AAC.05146-14.

[21] M.-X. Wei, J. Zhang, F.-L. Ma, M. Li, J.-Y. Yu, W. Luo, X.-Q. Li, Synthesis and biological activities of dithiocarbamates containing 2(5H)-furanone-piperazine, Eur. J. Med. Chem. 155 (2018) 165–170, doi:10.1016/j.ejmech.2018.05.056.

[22] B.N. Sağlık, Y. Özkay, Ü. Demir Özkay, H.K. Gençer, Synthesis and biological evaluation of some novel dithiocarbamate derivatives, J. Chem. 2014 (2014) 1–9, doi:10.1155/2014/387309.

[23] M. Mollazadeh, M. Mohammadi-Khanaposhtani, Y. Valizadeh, A. Zonouzi, M.A. Faramarzi, M. Kiani, M. Biglar, B. Larijani, H. Hamedifar, M. Mahdavi, M. H. Hajimiri, Novel coumarin containing dithiocarbamate derivatives as potent α-glucosidase inhibitors for management of type 2 diabetes, Med. Chem. (Los Angeles) 17 264–272.

[24] S.Z. Zard, The xanthate route to indolines, indoles, and their Aza Congeners, Chem. – Eur. J. 26 (2020) 12689–12705, doi:10.1002/chem.202001341.

[25] N. Kalgotra, B. Gupta, S. Andotra, S. Kumar, S.K. Pandey, Synthesis, spectral, thermal, electrochemical, and biocidal activity of tolyl/benzyl dithiocarbonates of Zinc(II), Int. J. Inorg. Chem. 2013 (2013) 1–12, doi:10.1155/2013/135496.

[26] R.F. Struck, W.R. Waud, Thiolo-, thiono- and dithiocarbonate and thiocarbamate derivatives of demethylpenclomedine as novel anticancer agents, Cancer Chemother. Pharmacol. 57 (2006) 180–184, doi:10.1007/s00280-005-0031-6.

[27] A. Rani, A comprehensive analysis of xanthates and their intrusion in different biological interaction, J. Res. Environ. Earth Sci. 2 (2015) 21–23.

[28] F. Carta, A. Akdemir, A. Scozzafava, E. Masini, C.T. Supuran, Xanthates and trithiocarbonates strongly inhibit carbonic anhydrases and show antiglaucoma effects in vivo, J. Med. Chem. 56 (2013) 4691–4700, doi:10.1021/jm400414j.

[29] A.A. Saboury, M. Alijanianzadeh, H. Mansoori-Torshizi, The role of alkyl chain length in the inhibitory effect n-alkyl xanthates on mushroom tyrosinase activities, Acta Biochim. Pol. 54 (2007) 183–191, doi:10.18388/abp.2007_3285.

[30] K. Rosenman, Benefits of saccharin: a review, Environ. Res. 15 (1978) 70–81, doi:10.1016/0013-9351(78)90080-4.

[31] L.M.T. Frija, E. Ntungwe, P. Sitarek, J.M. Andrade, M. Toma, T. Śliwiński, L. Cabral, M.L.S Cristiano, P. Rijo, A.J.L. Pombeiro, In vitro assessment of antimicrobial, antioxidant, and cytotoxic properties of Saccharin-Tetrazolyl and -Thiadiazolyl derivatives: the simple dependence of the pH value on antimicrobial activity, Pharmaceuticals (Basel) (2019) 12, doi:10.3390/ph12040167.

[32] A.A. Aly, S.A. Nassar, N-[4-(*dicyanomethylazo*)*phenyl*]-2-saccharin-2-ylacetamide in the synthesis of pyridazine and pyrimidine derivatives, Heteroat. Chem. 15 (2004) 2–8, doi:10.1002/hc.10194.

[33] O.I. El-Sabbagh, Synthesis of some new benzisothiazolone and benzenesulfonamide derivatives of biological interest starting from saccharin sodium, Arch. Pharm. 346 (2013) 733–742, doi:10.1002/ardp.201300110.

[34] P. Guglielmi, G. Rotondi, D. Secci, A. Angeli, P. Chimenti, A. Nocentini, A. Bonardi, P. Gratteri, S. Carradori, C.T. Supuran, Novel insights on saccharin- and acesulfame-based carbonic anhydrase inhibitors: design, synthesis, modelling investigations and biological activity evaluation, J. Enzyme Inhib. Med. Chem. 35 (2020) 1891–1905, doi:10.1080/14756366.2020.1828401.

[35] A. Csakai, C. Smith, E. Davis, A. Martinko, S. Coulup, H. Yin, Saccharin derivatives as inhibitors of interferon-mediated inflammation, J. Med. Chem. 57 (2014) 5348–5355, doi:10.1021/jm500409k.

[36] W.C. Groutas, L.S. Chong, R. Venkataraman, R. Kuang, J.B. Epp, N. Houser-Archield, H. Huang, J.R. Hoidal, Amino acid-derived phthalimide and saccharin derivatives as inhibitors of human leukocyte elastase, cathepsin G, and proteinase 3, Arch. Biochem. Biophys. 332 (1996) 335–340, doi:10.1006/abbi.1996.0350.

[37] P. Goel, T. Jumpertz, D.C. Mikles, A. Tichá, M.T.N. Nguyen, S. Verhelst, M. Hubalek, D.C. Johnson, D.A. Bachovchin, I. Ogorek, C.U. Pietrzik, K. Strisovsky, B. Schmidt, S. Weggen, Discovery and biological evaluation of potent and selective N-methylene saccharin-derived inhibitors for rhomboid intramembrane proteases, Biochemistry 56 (2017) 6713–6725, doi:10.1021/acs.biochem.7b01066.

[38] M. Trawally, K. Demir-Yazıcı, S.İ. Dingiş-Birgül, K. Kaya, A. Akdemir, Ö. Güzel-Akdemir, Mandelic acid-based spirothiazolidinones targeting M. tuberculosis: synthesis, in vitro and in silico investigations, Bioorg. Chem. 121 (2022) 105688, doi:10.1016/j.bioorg.2022.105688.

[39] P.K. Deb, N.A. Al-Shar'i, K.N. Venugopala, M. Pillay, P. Borah, In vitro anti-TB properties, in silico target validation, molecular docking and dynamics studies of substituted 1,2,4-oxadiazole analogues against Mycobacterium tuberculosis, J. Enzyme Inhib. Med. Chem. 36 (2021) 869–884, doi:10.1080/14756366.2021.1900162.

[40] A.T.K.B. Akhilesh, A. Uniyal, B. Das, R. Kumar, V. Tiwari, Structure-based virtual screening and molecular dynamics simulation for the identification of sphingosine kinase-2 inhibitors as potential analgesics, J. Biomol. Struct. Dyn. (2021) 1–19, doi:10.1080/07391102.2021.1971559.

[41] J. Ricci-Lopez, S.A. Aguila, M.K. Gilson, C.A. Brizuela, Improving structure-based virtual screening with ensemble docking and machine learning, J. Chem. Inf. Model. 61 (2021) 5362–5376, doi:10.1021/acs.jcim.1c00511.

[42] F. Stanzione, I. Giangreco, J.C. Cole, Use of molecular docking computational tools in drug discovery, Prog. Med. Chem. 60 (2021) 273–343, doi:10.1016/bs.pmch.2021.01.004.

[43] K. Park, A.E. Cho, Using reverse docking to identify potential targets for ginsenosides, J Ginseng Res 41 (2017) 534–539, doi:10.1016/j.jgr.2016.10.005.

[44] A. Ballesteros-Casallas, M. Paulino, P. Vidossich, C. Melo, E. Jiménez, J.-.C. Castillo, J. Portilla, G.P. Miscione, Synthesis of 2,7-diarylpyrazolo [1,5-a] pyrimidine derivatives with antitumor activity. Theoretical identification of targets _ Elsevier Enhanced Reader //Synthesis of 2,7-diarylpyrazolo [1,5-a] pyrimidine derivatives with antitumor activity. Theoretical identification of targets, Eur. J. Med. Chem. Rep. 4 (2022) 100028, doi:10.1016/j.ejmcr.2021.100028.

[45] A. Lee, K. Lee, D. Kim, Using reverse docking for target identification and its applications for drug discovery, Expert Opin. Drug Discov. 11 (2016) 707–715, doi:10.1080/17460441.2016.1190706.

[46] F. Chen, Z. Wang, C. Wang, Q. Xu, J. Liang, X. Xu, J. Yang, C. Wang, T. Jiang, R. Yu, Application of reverse docking for target prediction of marine compounds with anti-tumor activity, J. Mol. Graph. Model. 77 (2017) 372–377, doi:10.1016/j.jmgm.2017.09.015.

[47] X. Xu, M. Huang, X. Zou, Docking-based inverse virtual screening: methods, applications, and challenges, Biophys. Rep. 4 (2018) 1–16, doi:10.1007/s41048-017-0045-8.

[48] S. Tian, H. Sun, P. Pan, D. Li, X. Zhen, Y. Li, T. Hou, Assessing an ensemble docking-based virtual screening strategy for kinase targets by considering protein flexibility, J. Chem. Inf. Model. 54 (2014) 2664–2679, doi:10.1021/ci500414b.

[49] M.A. Ilies, D. Vullo, J. Pastorek, A. Scozzafava, M. Ilies, M.T. Caproiu, S. Pastorekova, C.T. Supuran, Carbonic anhydrase inhibitors. Inhibition of tumor-associated isozyme IX by halogenosulfanilamide and halogenophenylaminobenzolamide derivatives, J. Med. Chem. 46 (2003) 2187–2196, doi:10.1021/jm021123s.

[50] L.M. Harwood, C.J. Moody, P.B. Cranwell, ***Experimental Organic Chemistry***, John Wiley & Sons, Hoboken, New Jersey, 2017.

[51] L. Collins, S.G. Franzblau, Microplate alamar blue assay versus BACTEC 460 system for high-throughput screening of compounds against Mycobacterium tuberculosis and Mycobacterium avium, Antimicrob. Agents Chemother. 41 (1997) 1004–1009, doi:10.1128/AAC.41.5.1004.

[52] A. Chollet, L. Maveyraud, C. Lherbet, V. Bernardes-Génisson, An overview on crystal structures of InhA protein: apo-form, in complex with its natural ligands and inhibitors, Eur. J. Med. Chem. 146 (2018) 318–343, doi:10.1016/j.ejmech.2018.01.047.

[53] G. Macip, P. Garcia-Segura, J. Mestres-Truyol, B. Saldivar-Espinoza, M.J. Ojeda-Montes, A. Gimeno, A. Cereto-Massagué, S. Garcia-Vallvé, G. Pujadas, Haste makes waste: a critical review of docking-based virtual screening in drug repurposing for SARS-CoV-2 main protease (M-pro) inhibition, Med. Res. Rev. 42 (2022) 744–769, doi:10.1002/med.21862.

[54] E. Wang, H. Sun, J. Wang, Z. Wang, H. Liu, J.Z.H. Zhang, T. Hou, End-point binding free energy calculation with MM/PBSA and MM/GBSA: strategies and applications in drug design, Chem. Rev. 119 (2019) 9478–9508, doi:10.1021/acs.chemrev.9b00055.

[55] M.L. Benson, R.D. Smith, N.A. Khazanov, B. Dimcheff, J. Beaver, P. Dresslar, J. Nerothin, H.A. Carlson, Binding MOAD, a high-quality protein-ligand database, Nucleic. Acids. Res. 36 (2008) D674–D678, doi:10.1093/nar/gkm911.

[56] L. Hu, M.L. Benson, R.D. Smith, M.G. Lerner, H.A. Carlson, Binding MOAD (Mother Of All Databases), Proteins: Struct. Funct. Bioinform. 60 (2005) 333–340, doi:10.1002/prot.20512.

[57] Z.A. Rahima, S.N. Abdul Halim, F.N.-F. How, Crystal structure of S-(4-methylbenz-yl) piperidine-dithio-carbamate, Acta Cryst. E 71 (2015) o647, doi:10.1107/S2056989015014462.

[58] M. Akkurt, S. Karaca, E. Şahin, Ö. Güzel, A. Salman, O -Butyl S -(1,1,3-trioxobenz[*d*]isothiazol-2-yl)methyl dithiocarbonate, Acta Cryst. E 63 (2007) o2974-o2974, doi:10.1107/S160053680702363X.

[59] M. Ahmad, H.L. Siddiqui, M. Azam, I.H. Bukhari, M. Parvez, 2-(2-Oxo-2-phenyl-ethyl)-1,2-benziso-thia-zol-3(2H)-one 1,1-dioxide, Acta Crystallogr. Sect. E Struct. Rep. Online 66 (2010) o616, doi:10.1107/S1600536810005404.

[60] A.G. Orpen, L. Brammer, F.H. Allen, O. Kennard, D.G. Watson, R. Taylor, Appendix A: typical interatomic distances in organic compounds and organometallic compounds and coordination complexes of the D- and f-block metals, in: ***Structure Correlation***, John Wiley & Sons, Ltd, 2008, pp. 752–858.

[61] O.V. Dolomanov, L.J. Bourhis, R.J. Gildea, J.A.K. Howard, H. Puschmann, OLEX2 a complete structure solution, refinement and analysis program, J. Appl. Cryst. 42 (2009) 339–341, doi:10.1107/S0021889808042726.

[62] G.M. Sheldrick, A short history of SHELX, Acta Cryst. A 64 (2008) 112–122, doi:10.1107/S0108767307043930.

[63] L.J. Bourhis, O.V. Dolomanov, R.J. Gildea, J.A.K. Howard, H. Puschmann, The anatomy of a comprehensive constrained, restrained refinement program for the modern computing environment - Olex2 dissected, Acta Cryst. A 71 (2015) 59–75, doi:10.1107/S2053273314022207.

[64] A.L. Spek, PLATON SQUEEZE: a tool for the calculation of the disordered solvent contribution to the calculated structure factors, Acta Cryst. C 71 (2015) 9–18, doi:10.1107/S2053229614024929.

[65] M. Masetti, F. Falchi, D. Gioia, M. Recanatini, S. Ciurli, F. Musiani, Targeting the protein tunnels of the urease accessory complex: a theoretical investigation, Molecules 25 (2020) 2911, doi:10.3390/molecules25122911.